Unravelling the local structure of catalytic Fe-oxo clusters stabilized on the MOF-808 metal organic-framework

Celia Castillo-Blas,[1] Ignacio Romero-Muñiz,[1] Andreas Mavrandonakis,[2] Laura Simonelli,[3] Ana E. Platero-Prats*[1,4]

[1] Departamento de Química Inorgánica, Facultad de Ciencias, Universidad Autónoma de Madrid, Campus de Cantoblanco, 28049 Madrid, Spain.

[2] Electrochemical Processes Unit, IMDEA Energy, Avenida Ramón de la Sagra 3, 28935 Móstoles, Madrid, Spain.

[3] CLAESS beamline, ALBA Synchrotron, 08290 Cerdanyola del Vallès, Spain.

[4] Condensed Matter Physics Center (IFIMAC), Universidad Autónoma de Madrid, 28049, Campus de Cantoblanco, 28049 Madrid, Spain.

KEYWORDS. Insert here the keywords of the communication.

Supporting Information

S1 General information

All other reagents were used as received from commercial suppliers unless otherwise stated.

Powder X-ray diffraction (PXRD) patterns were measured with a Bruker D8 diffractometer with a copper source operated at 1600 W, with step size = 0.02° and exposure time = 0.5 s/step. Samples were placed on a borosilicate sample holder and then the sample surface was levelled with a clean microscope slide. All the samples were grinded prior to analysis unless otherwise stated. Data were measured using a continuous 2θ scan from 3.0-45º θ. For all samples, PXRD patterns are presented from 0–30º θ for visual clarity.

Scanning electron microscopy (SEM) images and **energy dispersive X-ray spectra** (EDS) were collected with an S-3000N microscope, equipped with an ESED and an INCAx-sight of Oxford Instruments, respectively. All samples were prepared for SEM and EDS by dispersing the material onto a double sided adhesive conductive carbon tape that was attached to a flat aluminum sample holder and were metallized with a gold layer of 15 nm with a Quórum Q150T-S sputter.

Field emission scanning electron microscopy (FE-SEM) observations were performed on a JSM 6335F microscope operating at 15 kV. All samples were prepared for FE-SEM by dispersing the material onto a double sided adhesive conductive carbon tape that was attached to a flat aluminum sample holder and were coated in C with a Sputter Coater Quorum, Q150T-S. Mapping were performed during 300 s with an INCAx X-Max of Oxford Instruments.

Nuclear magnetic resonance (NMR) spectra were acquired on a Bruker AV-300 spectrometer, running at 300 MHz for ^{1}H. Chemical shifts (δ) are reported in ppm relative to residual solvent signal with a value of 2.50 ppm for DMSO-d_6. ^{1}H digested solution NMR (300 µL DMSO-d_6, 50 µL D_2O, 50 µL HF, and 300 µL 5% D_2SO4 in DMSO-d_6 (v:v) solution) of as-synthesized sample MOF-808.

Textural analyses. Nitrogen adsorption and desorption isotherms were measured at 77 K using a Micromeritics ASAP 2020 system. The samples were outgassed at indicated temperature for 16 h before the measurements. The specific surface areas (BET) were calculated by application of the Brunauer-Emmett-Teller equation taking the area of the nitrogen molecule as 0.162 nm^2. The linear range of the BET equation was located between 0.05–0.35 P/P_0, however, for all other materials studied due to their microporous natures this linear range was much narrower and displaced to lower relative pressures: P/P_0= 0.015–0.1. The micropore volume and external surface area, *i.e.* the area not associated with the micropores, were calculated using a t-plot analysis. taking the thickness of an adsorbed layer of nitrogen as 0.354 nm and assuming that the arrangement of nitrogen molecules in the film was hexagonal close packed. The mesopore volumes of the materials were calculated from the volume of gas adsorbed at a relative pressure of 0.6 on the desorption branch of the isotherms, equivalent to the filling of all pores below 50 nm, minus the microporosity calculated from the corresponding t-plot. The total pore volume was calculated from the volume of gas adsorbed at a relative pressure of 0.95 on the absorption branch of the isotherms. The pore-size-distribution (PSD) curves were obtained from the adsorption branches using non-local density functional theory (NLDFT) method for a cylinder pore in pillared clays, using a regularization of 0.00316.

Thermogravimetric analyses and **differential thermal analyses** (TGA-DTA) were performed using a SDT Q600 from TA Instruments equipment in a temperature range between 40 °C and 800 °C in air (100 mL/min flow) atmosphere and heating rate of 10 ºC/min.

Infrared spectra (FTIR) were recorded on a PerkinElmer 100 spectrophotometer using a PIKE Technologies MIRacle Single Reflection Horizontal ATR Accessory from 4000-450 cm^{-1}.

Elemental analyses were performed with a LECO CHNS-932 analyser, with dry samples.

ICP analyses were performed with an Inducted Coupled Plasma Emission Spectrometer ICP PERKIN ELMER mod. OPTIMA 2100 DV. Samples were digested in 5 mL of a 1:1 H_2O_2:H_2SO_4 mixture (v:v) and taken to a 15 mL volume with distilled water.

S2 Synthesis of the materials

MOF-808. Trimesic acid (117 mg, 0.55 mmol) was added to a stirred suspension of zirconyl chloride octahydrate (539 mg, 1.6 mmol) in DMF (45 mL) and formic acid (45 mL) in a screwed bottle. The reaction was heated at 130 ºC for 48 h (aprox.) in the oven. The reaction mixture was centrifuged, and the solid was washed with DMF, water and acetone three times each. The solid was dried under ambient pressure yielding MOF 808 as a white powder. The powder was treated with supercritical CO_2 (SC-CO_2) and dried under dynamic vacuum 4 hours at room temperature and 100 °C overnight. Yield: 405.7 mg, 85% based on Zr). EA of sample: Calcd. For $Zr_6C_{24.5}H_{64.5}N_{1.5}O_{47.5}$ = $[Zr_6O_4(OH)_6(C_9H_3O_6)_2(COOH)_2(C_3H_7NO)_{1.5}(H_2O)_{20}]$: C 17.44%, H 3.82%, N 1.25%; Found: C 17.57%, H 4.10%, N 1.31%. 8.56 (s, 3H, 1 × BTC), 8.02 (s, 2H, 2 × HCOOH), 7.84 (s, 1H, 1.5 × DMF), 2.85 (s, 3H, 1.5 × DMF), 2.69 (s, 3H, 1.5 × DMF).

Fe-0.5-MOF-808. A mixture of MOF-808 (100 mg, 0.074 mmol), $FeCl_2{\cdot}4H_2O$ (180 mg, 0.905 mmol) and 10 mL of DMF was placed in a sealed vial. The solution was stirred at 60 °C for 24 h. After cooling, the reaction was allowed to cool to room temperature. Light yellow powder was collected by centrifugation (8,000 rpm, 2 min), washed with DMF, water and with acetone three times each. The solid was dried under ambient pressure yielding FeMOF-808 as an orangish powder. The powder was treated with supercritical SC-CO_2 and dried under dynamic vacuum 4 hours at room temperature and 60°C overnight. Yield: 97.2 mg, 71% based on Zr. ICP ratio Fe/Zr_6: 0.0833. EA of sample: Calcd. For $Fe_{0.5}Zr_6C_{24.5}H_{74.5}N_{1.5}O_{52.5}Cl_{1.5}$ = $[Fe_{0.5}Zr_6O_4Cl_{1.5}(OH)_6(C_9H_3O_6)_2(COOH)_2(C_3H_7NO)_{1.5}(H_2O)_{25}]$: C 15.83%, H 4.04%, N 1.13%; Found: C 15.99%, H 4.20%, N 1.40%.

Fe-1.2-MOF-808. A mixture of MOF-808 (100mg, 0.074 mmol), $FeCl_2{\cdot}4H_2O$ (360mg, 1.810 mmol) and 10mL of DMF was placed in a sealed vial. The solution was stirred at 60 °C for 24h. After cooling, the reaction was allowed to cool to room temperature. Light yellow powder was collected by centrifugation (8,000 rpm, 2 min), washed with DMF, water and with acetone three times each. The solid was dried under ambient pressure yielding FeMOF-808 as an orange powder. The powder was treated with supercritical SC-CO_2 and dried under dynamic vacuum 4 hours at room temperature and 60 °C overnight. Yield: 94.2 mg, 69% based on Zr. ICP ration Fe/Zr_6: 0.2. EA of sample: Calcd. For $Fe_{1.2}Zr_6C_{23}H_{61}NO_{47}Cl_{3.6}$ = $[Fe_{1.2}Zr_6O_4Cl_{3.6}(OH)_6(C_9H_3O_6)_2(COOH)_2(C_3H_7NO)(H_2O)_{20}]$: C 14.97%, H 3.33%, N 0.76%; Found : C 15.22%, H 3.99%, N 0.58%.

Water molecules are removed from the pores under dynamic vacuum at 150 ºC. However, with the pass of the time these molecules can be re-adsorpted in the pores.

S3 Scanning Electron Microscopy. Energy Dispersing X-ray Spectroscopy

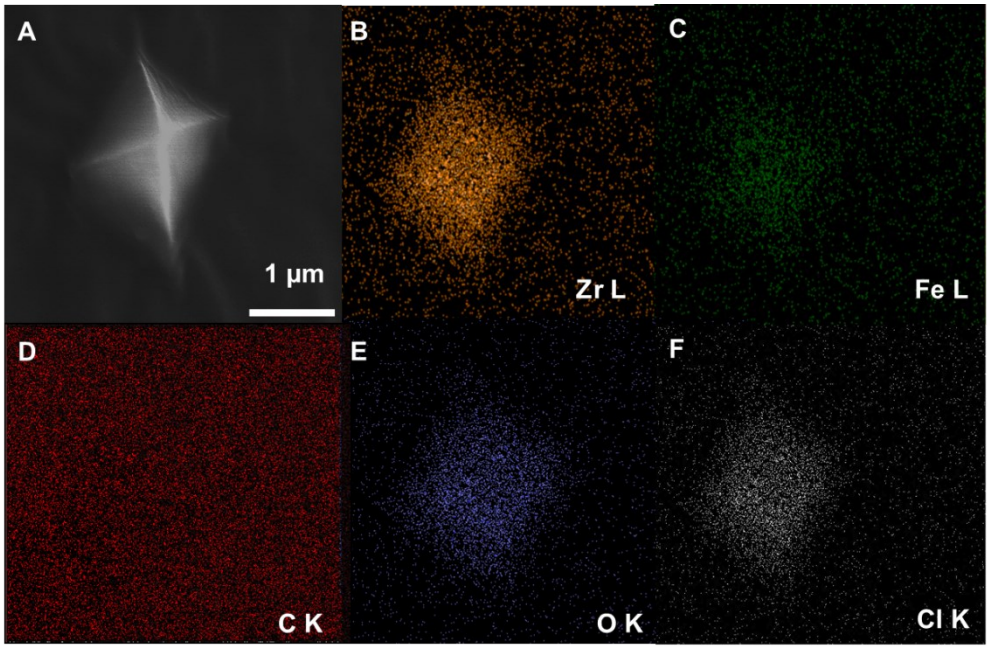

Fig S3.1. Mapping Fe-0.5-MOF-808. Accumulating images (A) and corresponding elemental mappings of (B) Zr, (C) Fe, (D) C, (E) O and (F) Cl.

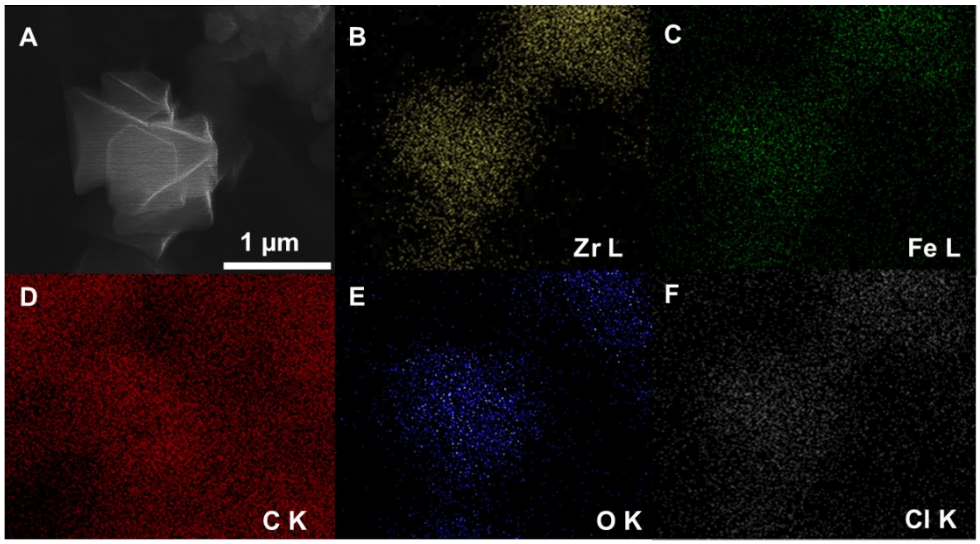

Fig S3.2. Mapping Fe-1.2-MOF-808. Accumulating images (A) and corresponding elemental mappings of (B) Zr, (C) Fe, (D) C, (E) O and (F) Cl.

Mapping images show the presence of all the elements in the crystallites. Zirconium, chlorine and iron are homogeneously distributed in the octahedral crystals.

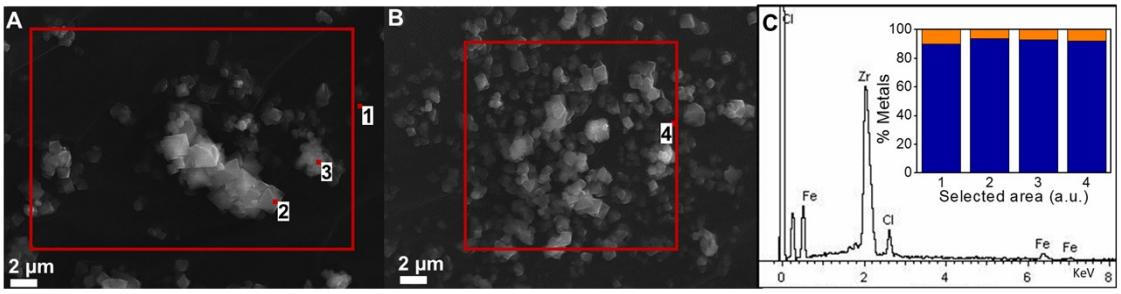

Fig S3.3. SEM-EDS analyses of Fe-0.5-MOF-808. Red spots in A and B indicate the areas where EDS where performed. Spectrum is depicted in C and the inset plot shows the Metals % (%Fe (orange), %Zr (blue).) by EDS analyses, where each column corresponds to the area indicated by a number in the SEM pictures A and B.

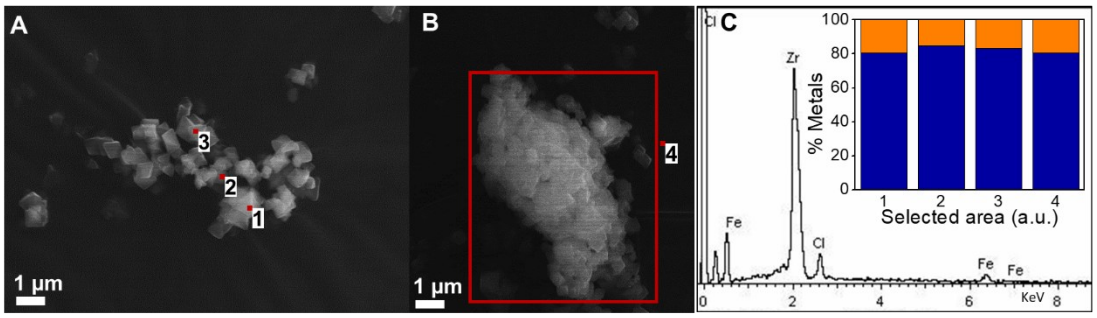

Fig S3.4. SEM-EDS analyses of Fe-1.2-MOF-808. Red spots in A and B indicate the areas where EDS where performed. Spectrum is depicted in C and the inset plot shows the Metals % (%Fe (orange), %Zr (blue).) by EDS analyses, where each column corresponds to the area indicated by a number in the SEM pictures A and B.

SEM images present crystallites with a size between 0.5-1 µm and homogenous shape of octahedron. The distribution of the iron and the zirconium is homogenous.

Metal incorporation of Fe on the $Zr_6O_8H_4$ SBUs was tested by anion and time condition screening. The experiments was monitored by FE-SEM-EDS (Table S3.1 ans Table S3.2) based on the Fe/Zr ration of each sample. The objetive of the tests were to see a global picture on the incorporation of Fe in a second shell of the Zr-oxo cluster:

S3.1. Metal incorporation tests

Metal incorporation of Fe on the $Zr_6O_8H_4$ SBUs was tested by anion and time condition screening. The counterion test was developed with following the same conditions in all cases. A mixture of MOF-808 pristine (10 mg, 7 mmol), iron salt (70 mmol) and 5 mL of DMF was placed in a sealed vial. The solution was stirred at 60 °C for 16 h, in a general way. After cooling, the reaction was allowed to cool to room temperature. Light yellow powder was collected by centrifugation (8,000 rpm, 2 min), washed with DMF, water and with acetone three times each. The resultant solids were dried under dynamic vacuum. The experiments was monitored by FE-SEM-EDS (Table S3.1) based on the Fe/Zr ration of each sample. The objetive of the tests were to see a global picture on the incorporation of Fe in a second shell of the Zr-oxo cluster:

Table S3.1: optimization parameters of the Zr-oxo metallation:

Metal precursor	Time / h	Zr_6:Fe ratio	%Fe	Error / %
$FeCl_3$	16	0	0	0.0
$Fe(NO_3)_3$	16	0	0	0.0
$Fe(acac)_3$	16	0.79	11.6	3.5
$Fe(ox)_2$	16	2.29	27.5	13.9
$Fe(AcO)_2$	16	0.66	9.9	13.1
$FeCl_2$	0.03	0.92	13.35	0.66
$FeCl_2$	0.15	0.94	13.57	6.47
$FeCl_2$	0.5	1.48	19.81	1.93
$FeCl_2$	1	1.96	24.58	1.64
$FeCl_2$	2	0.45	6.93	0.61
$FeCl_2$	16	0.84	12.3	1.0
$FeCl_2$	160	0.52	8.03	0.96

[a] Referred to SEM-EDS values

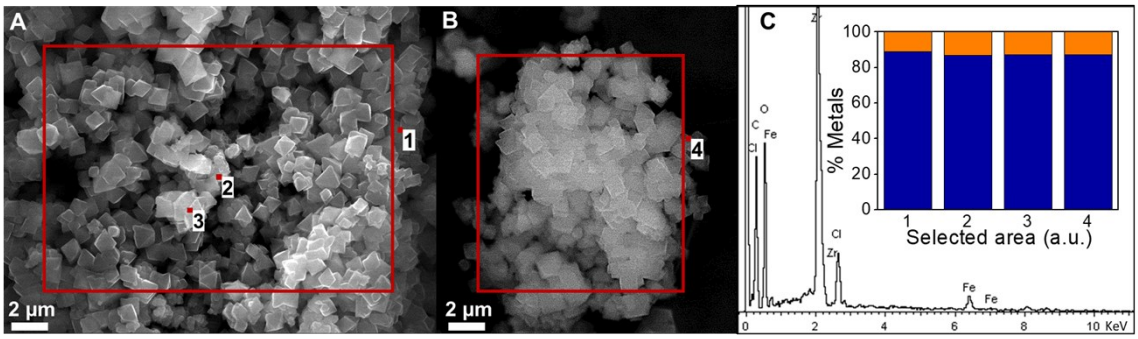

Fig S3.5. SEM-EDS analyses of $FeCl_2$-MOF-808. Red spots in A and B indicate the areas where EDS where performed. Spectrum is depicted in C and the inset plot shows the Metals % (%Fe (orange), %Zr (blue).) by EDS analyses, where each column corresponds to the area indicated by a number in the SEM pictures A and B.

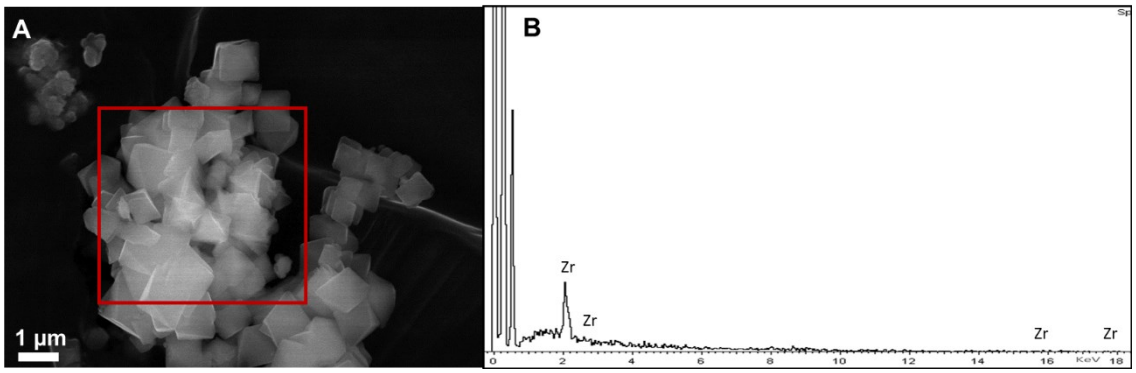

Fig S3.6. SEM-EDS analyses of $FeCl_3$-MOF-808. Red line in A delimits the area where EDS where performed. Spectrum is depicted in B.

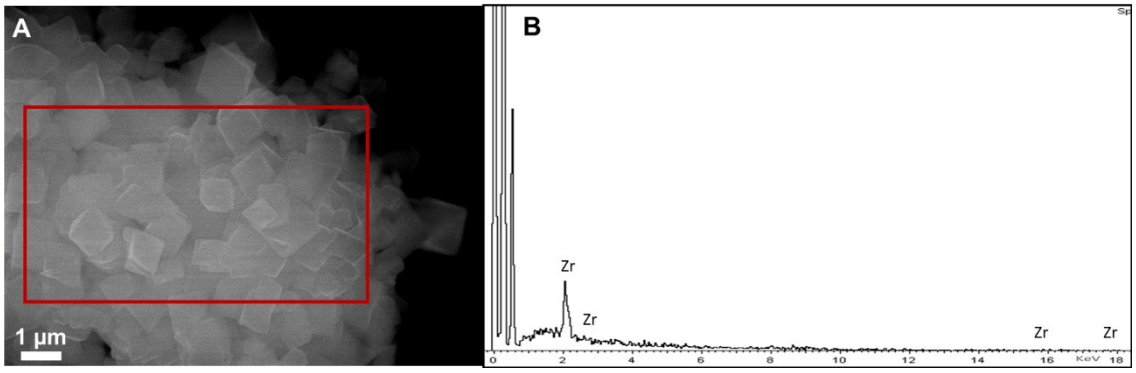

Fig S3.7. SEM-EDS analyses of $Fe(NO_3)_3$-MOF-808. Red line in A delimits the area where EDS where performed. Spectrum is depicted in B.

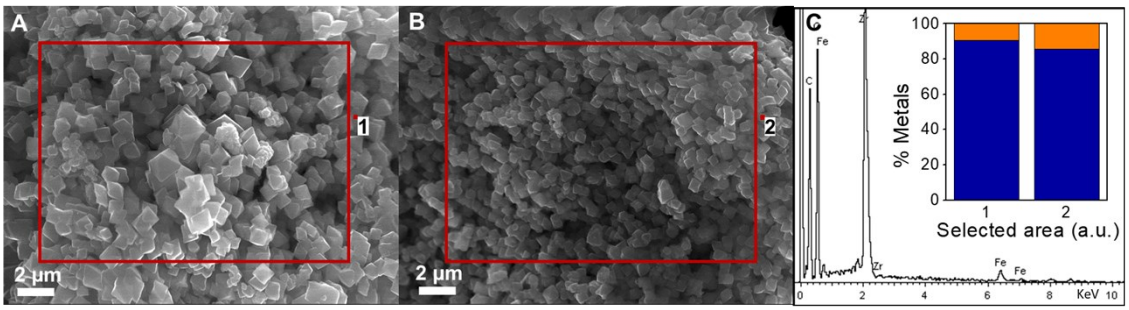

Fig S3.8. SEM-EDS analyses of $Fe(acac)_3$-MOF-808. Red spots in A and B indicate the areas where EDS where performed. Spectrum is depicted in C and the inset plot shows the Metals % (%Fe (orange), %Zr (blue).) by EDS analyses, where each column corresponds to the area indicated by a number in the SEM pictures A and B.

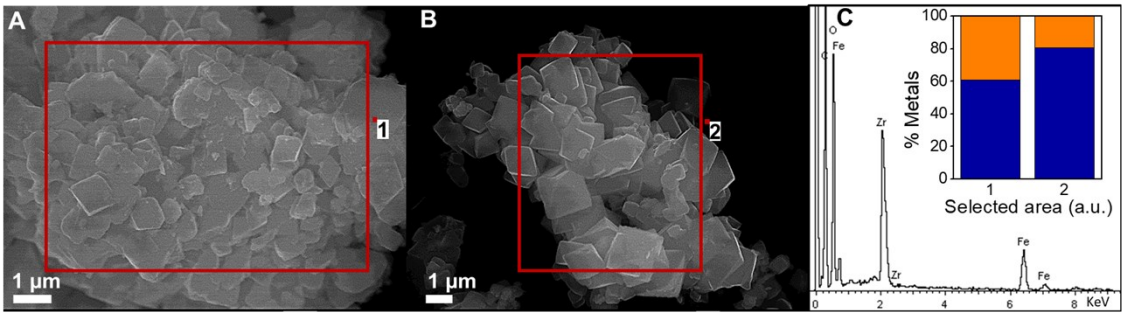

Fig S3.9. SEM-EDS analyses of $Fe(ox)_2$-MOF-808. Red spots in A and B indicate the areas where EDS where performed. Spectrum is depicted in C and the inset plot shows the Metals % (%Fe (orange), %Zr (blue).) by EDS analyses, where each column corresponds to the area indicated by a number in the SEM pictures A and B.

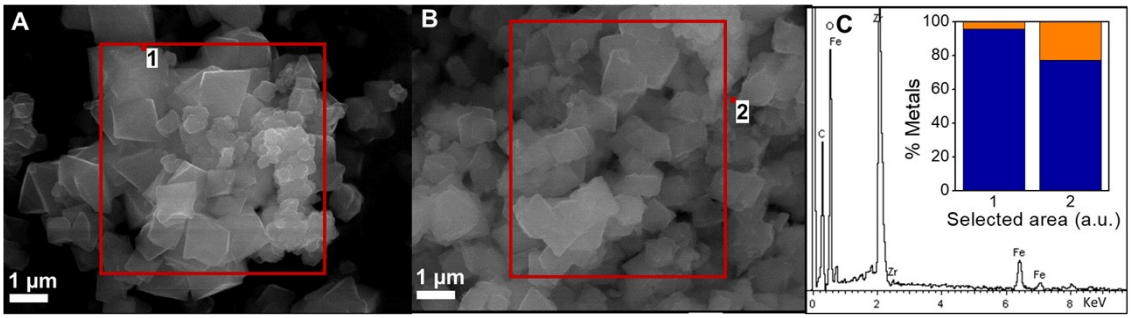

Fig S3.10. SEM-EDS analyses of $Fe(Ac)_2$-MOF-808. Red spots in A and B indicate the areas where EDS where performed. Spectrum is depicted in C and the inset plot shows the Metals % (%Fe (orange), %Zr (blue).) by EDS analyses, where each column corresponds to the area indicated by a number in the SEM pictures A and B.

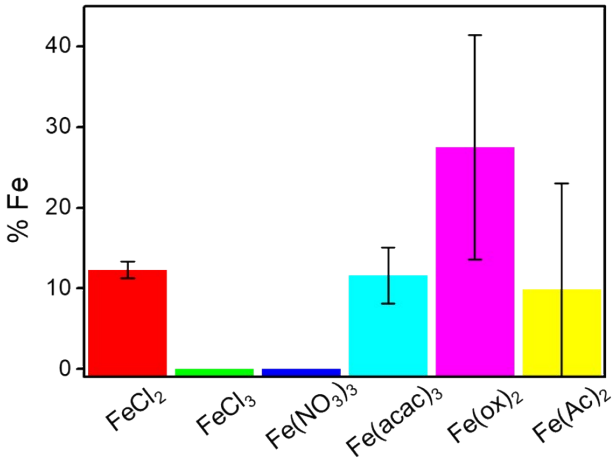

Fig S3.11. Summary of the study of the counterion with their corresponding error bars in the EDS analyses.

We can observe different influence of the counterion employed in the synthesis and the iron amount incorporated in the MOF-808. The use of $FeCl_3$ and $Fe(NO_3)_3$ suggest the incorporation of iron is not effective, while with $Fe(acac)_3$, $Fe(Ac)_2$ and $Fe(ox)_2$ is more effective. However, the distribution of Fe amount in the different crystallites is heterogeneous. Thus, the $FeCl_2$ is selected as iron precursor in these impregnation experiments.

S4 Nitrogen adsorption-desorption analyses

The BET analysis of the materials show a disminution of the specific surface area of metalated materials. Regarding to the NLDFT pore size distribution calculation, the Fe-loaded MOFs seems to maintain the micropore windown (*ca.* 12 Å and *ca.*18 Å) but the micropore contribution (take as the pore width under 22 Å) to the total pore volume rapidly decrease with the metal lodaing. Data collected from the t-plot analysis show an increment in the external surface area of the Fe-1.2-MOF-808 (34 m^2g^{-1} in the presitine and 175 m^2g^{-1} in the high concentrated sample)

Table S4.1. Data collected from N_2 isotherms at 77K, BET and t-plot analysis

Sample	Heat treatment	Surface area (BET) / m^2g^{-1}	External area / m^2g^{-1}	Micropore volume / cm^3g^{-1}	Mesopore volume / cm^3g^{-1}	Total pore volume / cm^3g^{-1}
MOF808-P	100ºC	1548	34	0.62	0.03	0.72
Fe-0.5-MOF808	60ºC	896	21	0.31	0.02	0.37
Fe-1.2-MOF808	60ºC	619	175	0.17	0.13	0.37

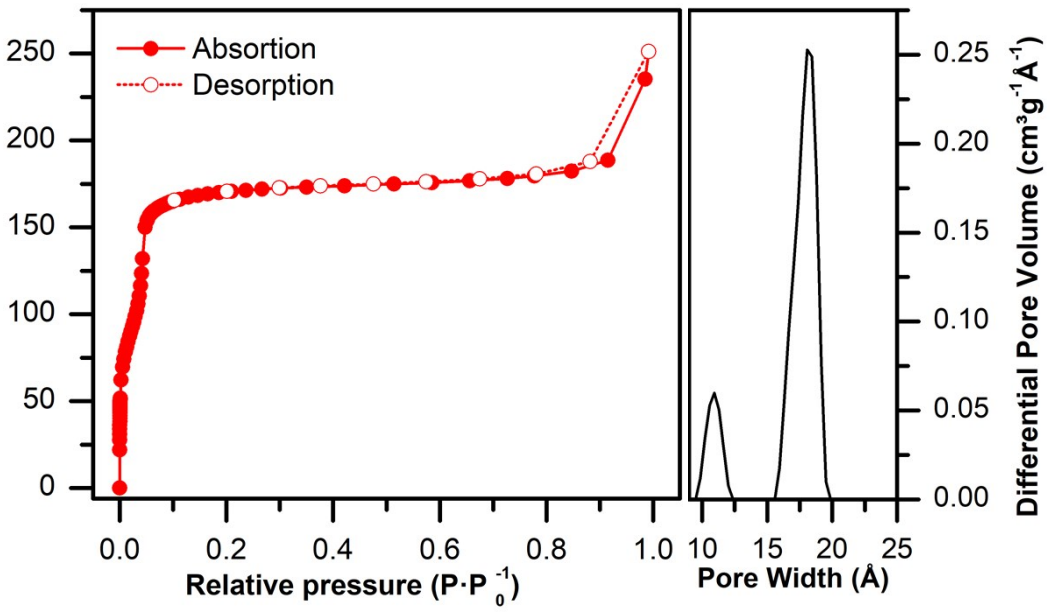

Fig. S4.1. N_2 isotherm, BET analysis and DFT pore size distribution of MOF-808 pristine.

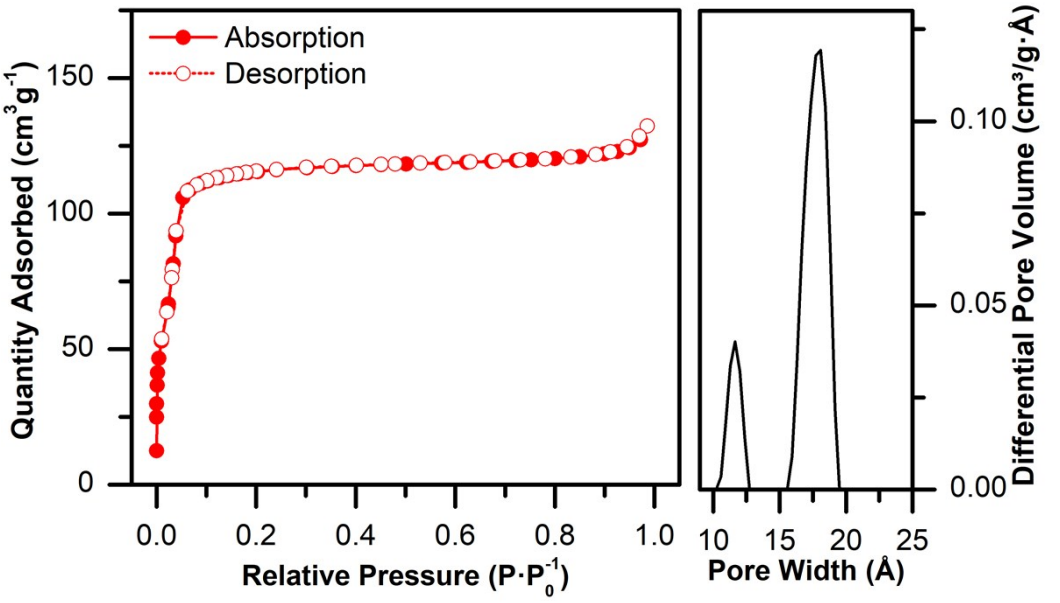

Fig. S4.2. N_2 isotherm, BET analysis and NLDFT pore size distribution of Fe-0.5-MOF-808.

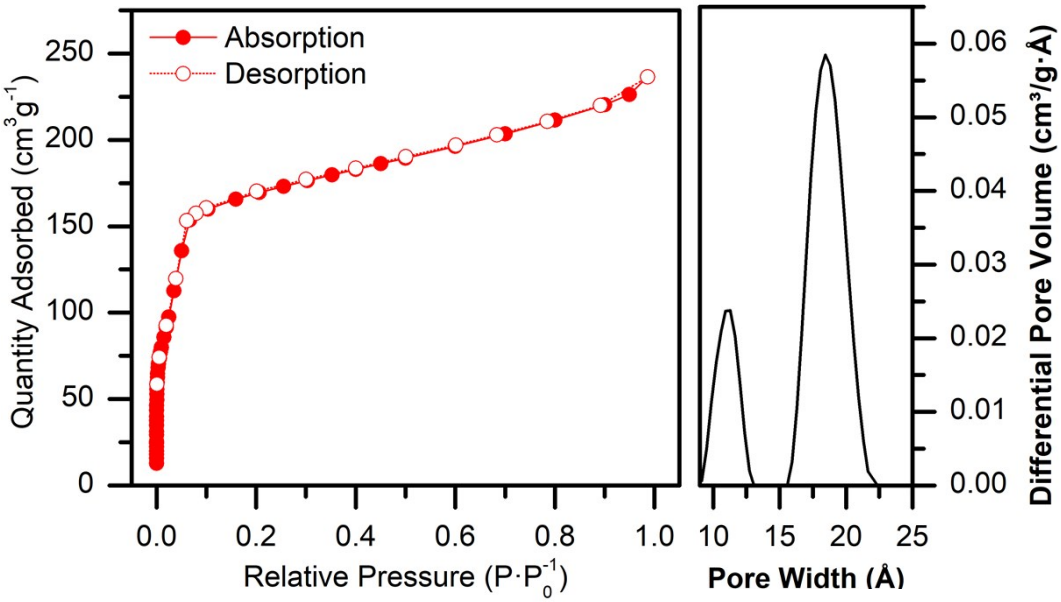

Fig. S4.3. N_2 isotherm, BET analysis and NLDFT pore size distribution of Fe-1.2-MOF-808.

S5 Thermal gravimetric analysis

TGA data collected on all the materials showed a mass loss associated with loss of water molecules with values of 31.9%, 34.3% and 14.3% for MOF-808, Fe-0.5-MOF-808 and Fe-1.2-MOF-808, respectively. This first curve is more pronounced in the Fe-0.5-MOF-808, than pristine MOF due to the amount of water which this material possesses, according to EA. Additionally, we can observe that the pristine MOF-808 and Fe-1.2-MOF-808 have two steps in their TGA curves.

The residues of these materials correspond to 43.5, 40.4 and 34.8% for MOF-808, Fe-0.5-MOF-808 and Fe-1.2-MOF-808, respectively. These residues are identified as ZrO_2 in all the cases.

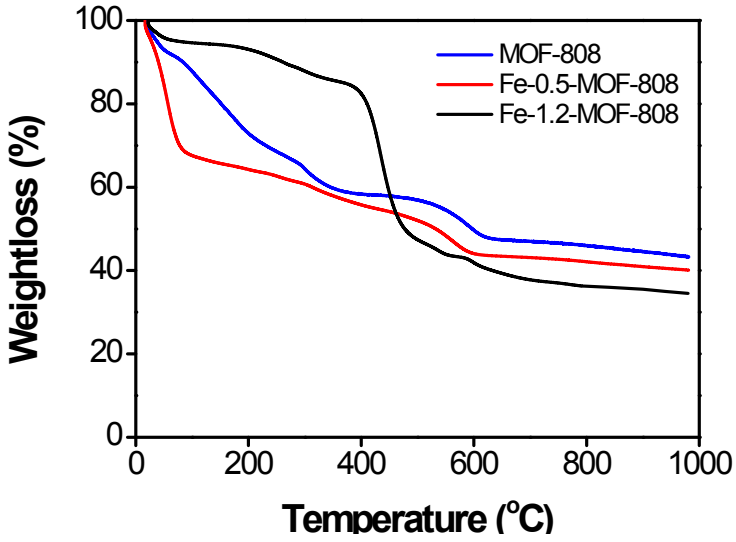

Fig. S5.1. Thermogravimetric analyses of materials.

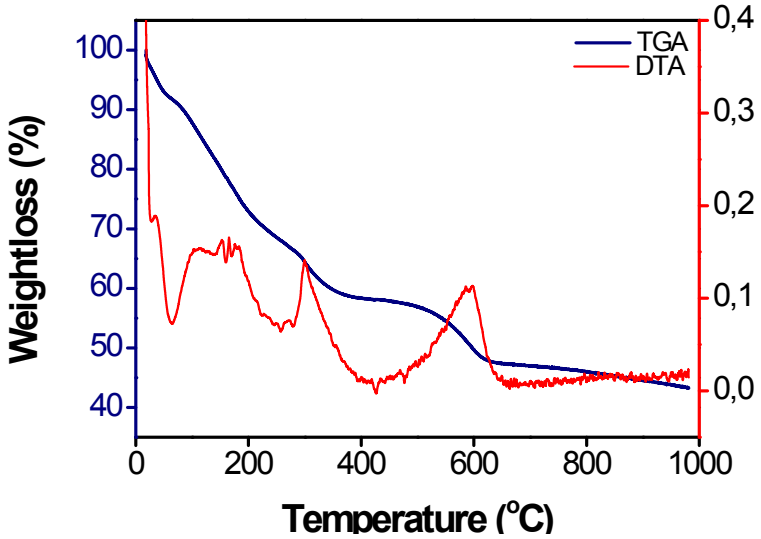

Fig. S5.2. Thermogravimetric analysis and differential thermal analysis of MOF-808.

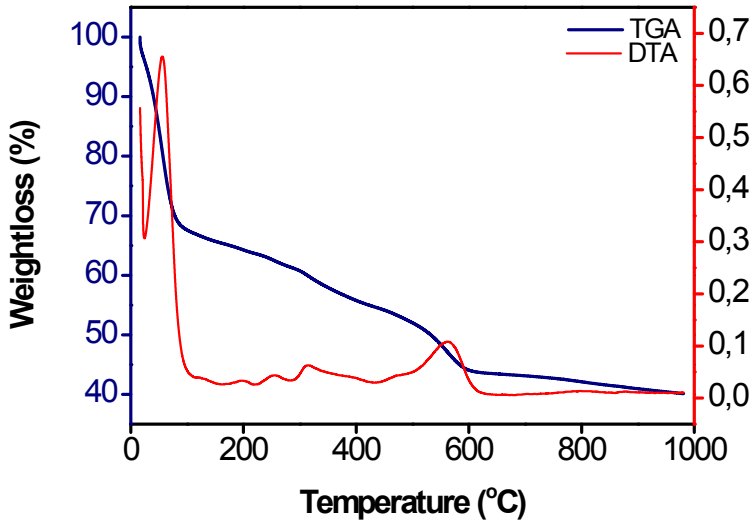

Fig. S5.3. Thermogravimetric analysis and differential thermal analysis of Fe-0.5-MOF-808.

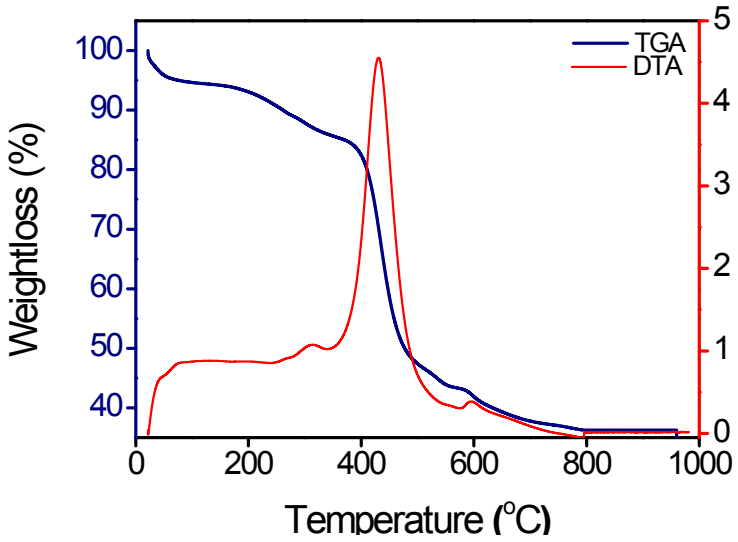

Fig. S5.4. Thermogravimetric analysis and differential thermal analysis of Fe-1.2-MOF-808.

S6 ATR-FTIR analysis

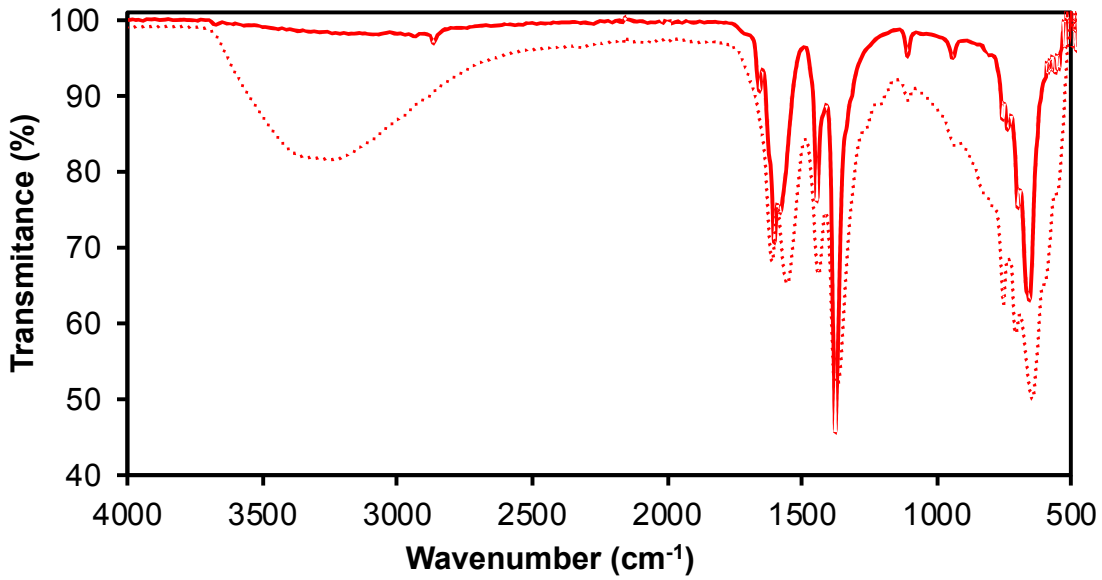

Fig. S6.1. ATR-FTIR of MOF-808 before (solid) and after catalysis (dashed).

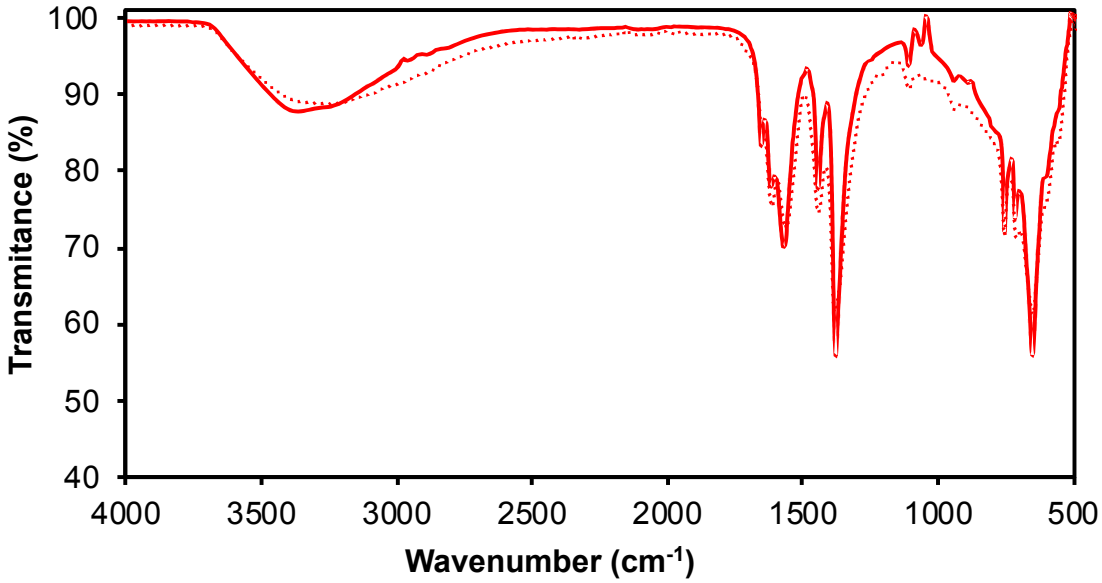

Fig. S6.2. ATR-FTIR of Fe-0.5-MOF-808 before (solid) and after catalysis (dashed).

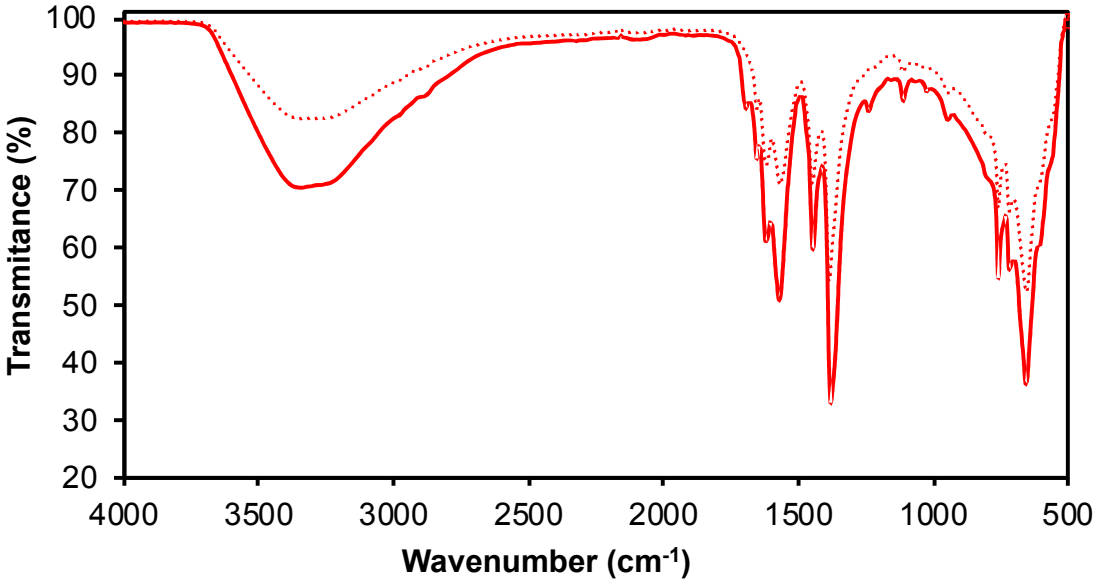

Fig. S6.3. ATR-FTIR of Fe-1.2-MOF-808 before (solid) and after catalysis (dashed).

S7 X-ray powder diffraction

X-ray diffraction patterns of the materials show a high crystallinity and pure phases compared with the calculated pattern from single crystal data.[1] According to Pawley refinements, impregnated materials present a small 0.425 and 0.899-shift, with the corresponding expansion of the unit cell until 34.73928 and 35.21372 Å for Fe-0.5-MOF-808 and Fe-1.2-MOF-808, respectively (Table S7.1 and Fig S7.2-S7.4). This is consistent with other examples of impregnation of metals in MOFs,[2] due to this new metal clusters are located in the pores, expanding the crystalline structure.

A loss of crystallinity is observed in Fe-0.5-MOF-808 after catalysts. This is expected, as the high oxidant conditions (see section S11) employed during catalysis (Fig S7.5).[3]

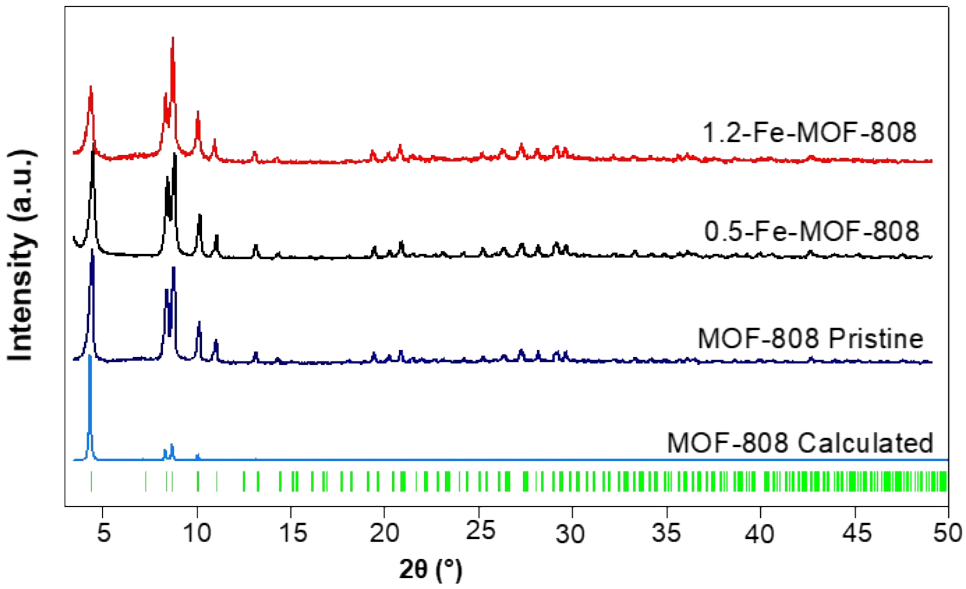

Fig S7.1. X-ray powder diffraction patterns of materials and their comparison with the calculated MOF-808 reported by Yaghi *et al*.[1] Bragg positions are depicted as green vertical lines.

Table S7.1. Pawley refinement values for synthetized samples.

Sample	a	R_{wp}	R_p	Zero	U	V	W
MOF-808 Pristine	34.3145 (3)	1.10%	0.77%	0.0491 (3)	-0.0090 (2)	-0.0247 (4)	0.0204 (3)
Fe-0.5-MOF-808	34.7392 (2)	0.52%	0.36%	0.0524 (2)	-0.0014 (3)	-0.0345 (3)	0.0157 (3)
Fe-1.2-MOF-808	35.2137 (2)	0.53%	0.34%	0.0518 (5)	-0.0010 (2)	-0.0292 (2)	0.0132 (2)

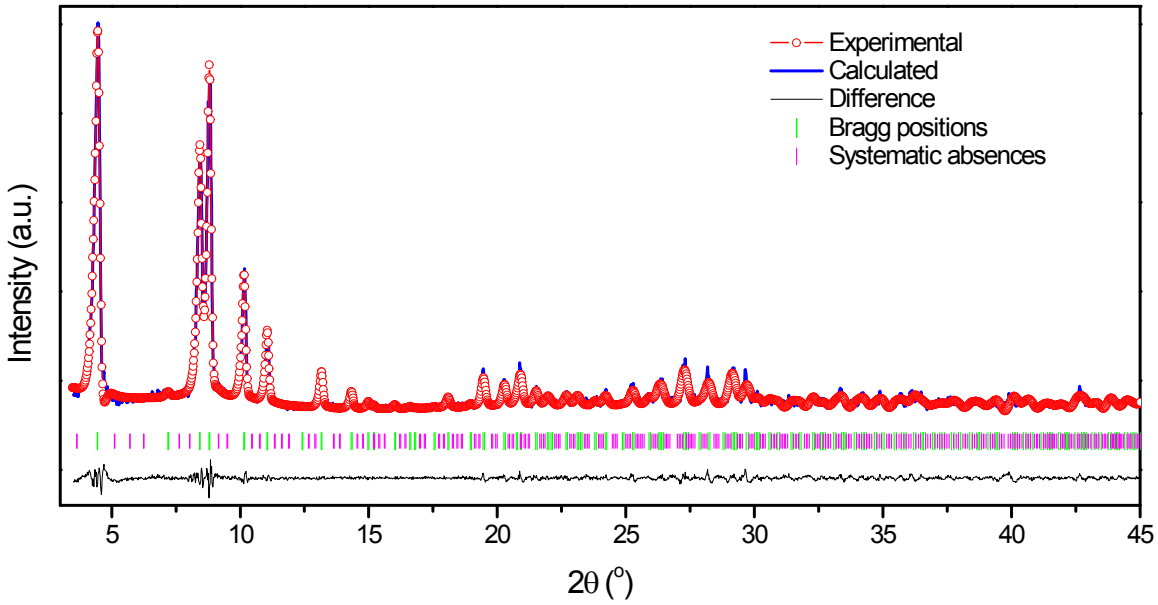

Fig S7.2. Pawley refinement for MOF-808 pristine.

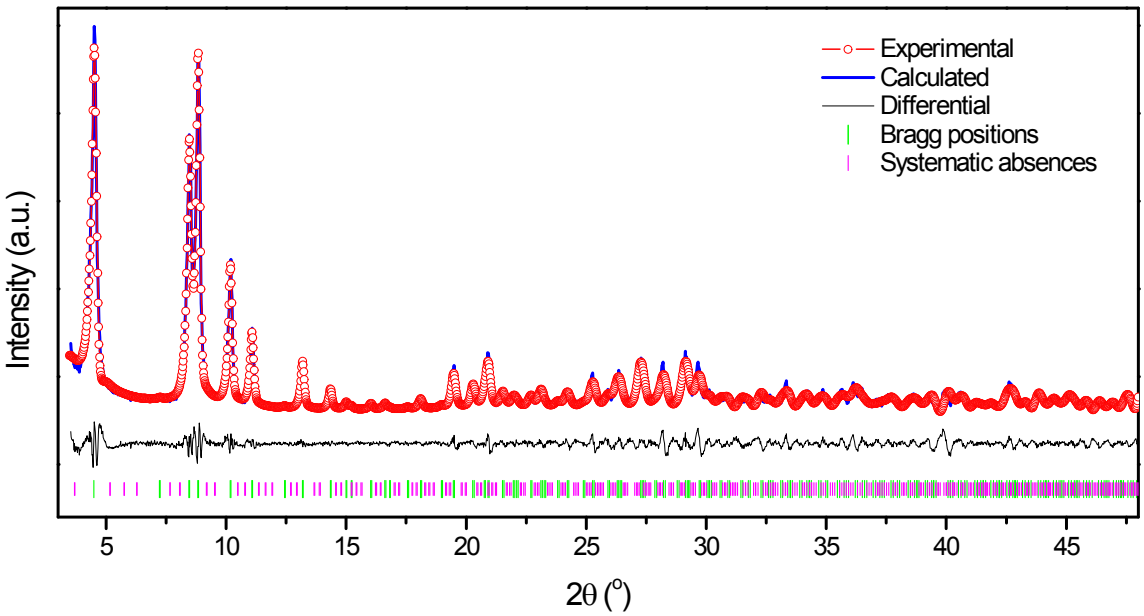

Fig S7.3. Pawley refinement for Fe-0.5-MOF-808.

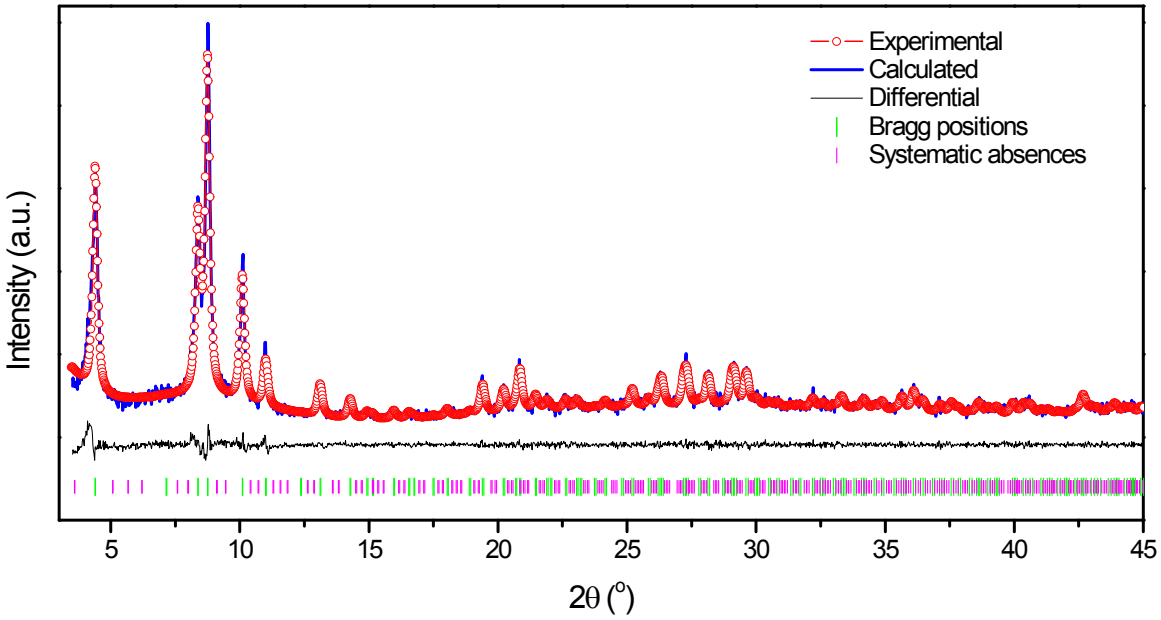

Fig S7.4. Pawley refinement for Fe-1.2-MOF-808.

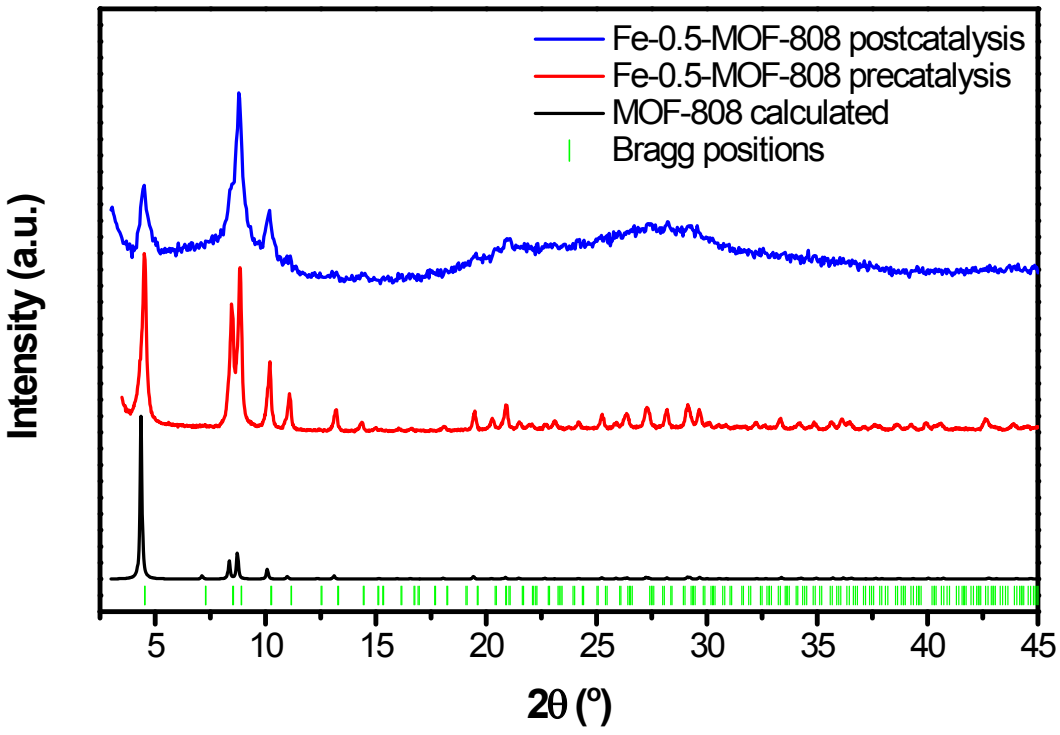

Fig S7.5. X-ray powder diffraction patterns of materials and their comparison with the calculated MOF-808. Bragg positions are depicted as green vertical lines.

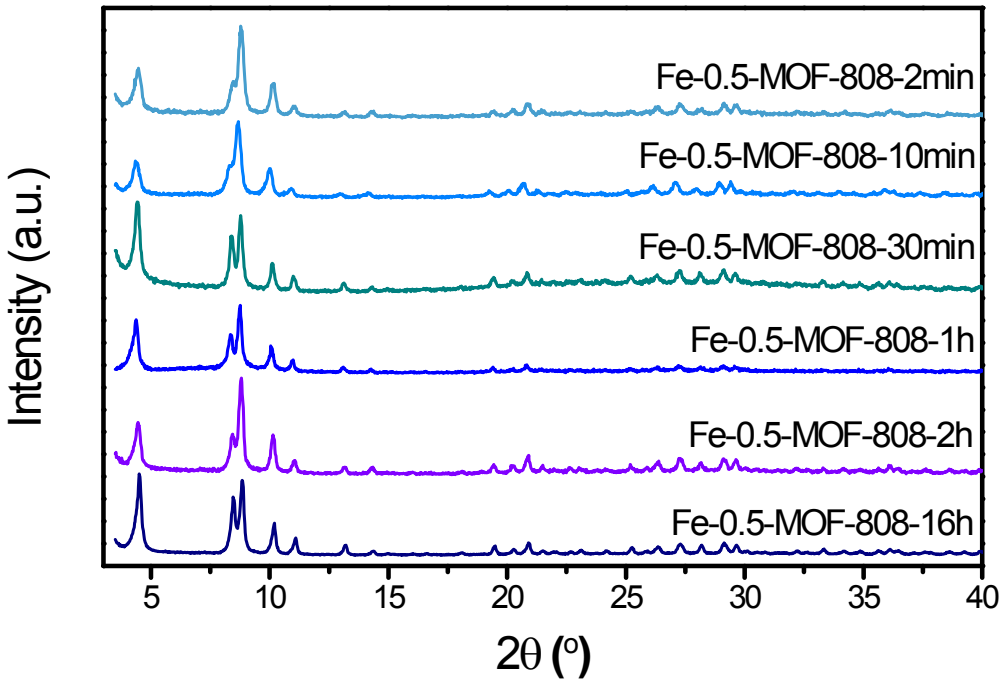

Fig S7.6. X-ray powder diffraction patterns of prepared materials at different reaction time of Fe-impregnation.

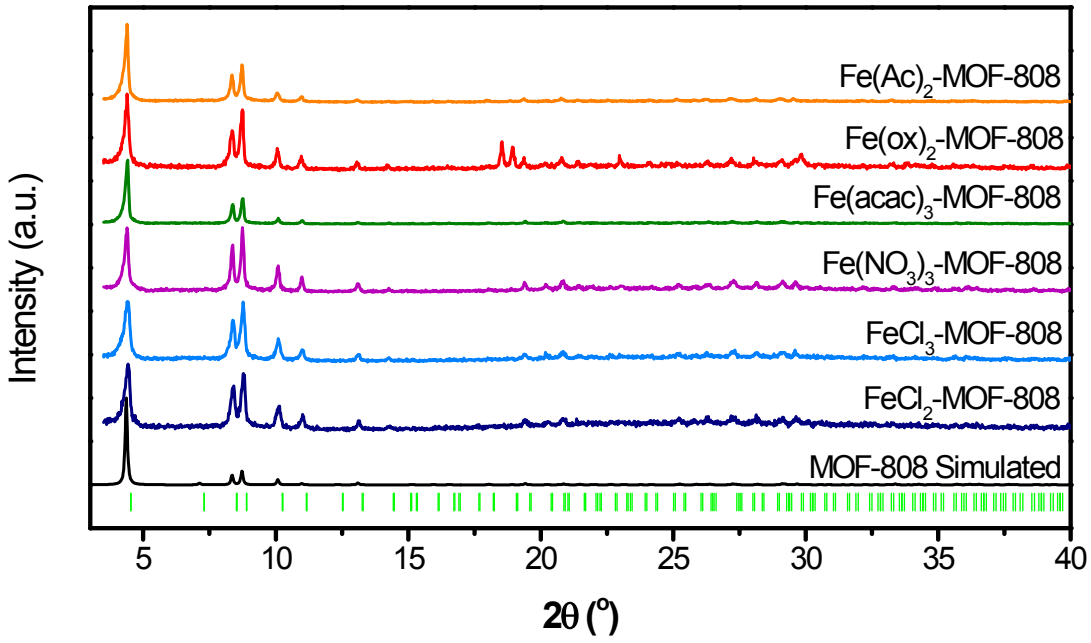

Fig S7.7. X-ray powder diffraction patterns of prepared materials with different iron-precursors of Fe-impregnation.

S8 Pair Distribution Function

Synchrotron X-ray total scattering data suitable for PDF analyses were collected at the P02.1 beamline at PETRA IIII (Deutsches Elektronen-Synchrotron) using 60 keV (0.207 Å) X-rays. Samples were loaded in polyamide (kapton) capillaries (0.8 mm Ø) and sealed using epoxy. Data were collected using an amorphous silicon–based PerkinElmer area detector. Geometric corrections and reduction to 1D data used DAWN Science software.[4] PDFs were obtained from the data within PDFgetX3 within xPDFsuite to a Qmax = 22 $Å^{-1}$.[5] Differential PDFs were obtained by subtraction of a reference PDF (MOF-808 pristine) from Fe-MOF-808 in real space using Microsoft Excel. The control was multiplied by an appropriate constant to ensure that the scale of each PDF was the same. Interatomic distances were quantified by fitting Gaussian functions using Fityk software.[6] Preliminary models of iron clusters were performed in Materials Studio 2017.[7] PDFs for structural models of iron clusters were simulated within PDFgui.[8]

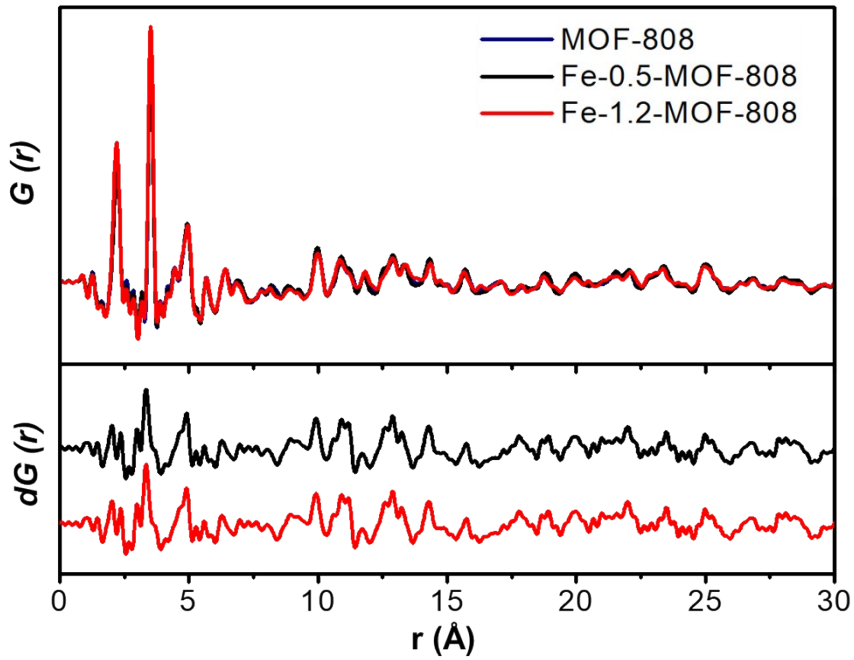

Fig. S8.1. (Up) PDF patterns for the different materials Fe-1.2-MOF-808, Fe-0.5-MOF-808 and MOF-808 pristine. (Down) Differential patterns for Fe-1.2-MOF-808 and Fe-0.5-MOF-808.

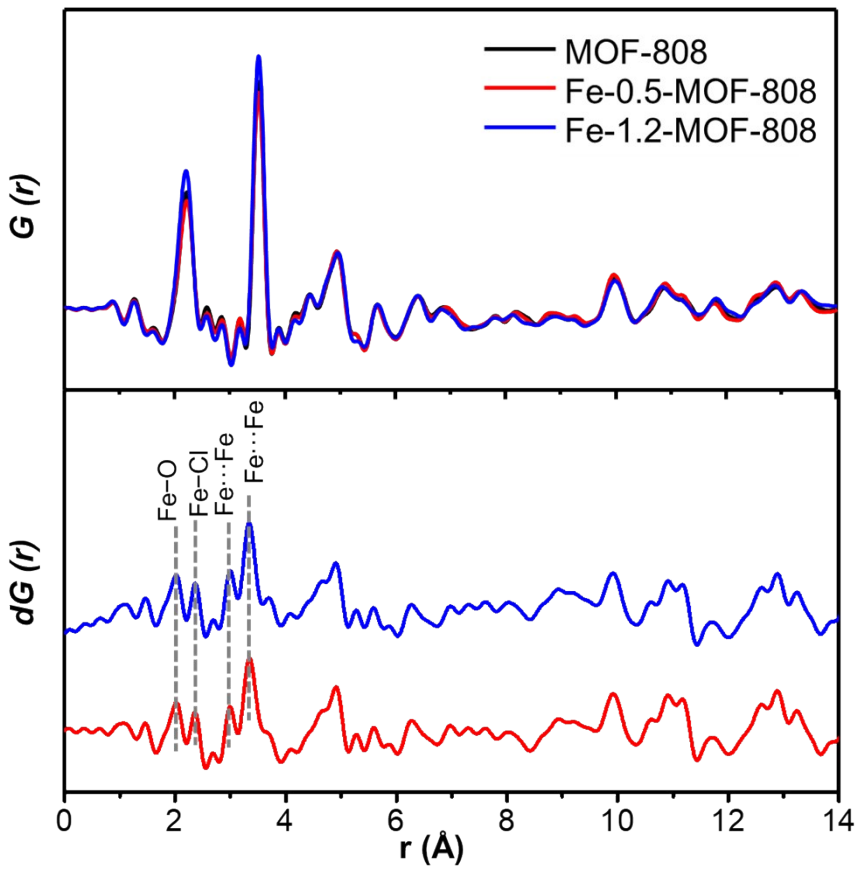

Fig. S8.2. Zoom of figure S8.1. (Up) PDF patterns for the different materials Fe-1.2-MOF-808, Fe-0.5-MOF-808 and MOF-808 pristine. (Down) Differential patterns for Fe-1.2-MOF-808 and Fe-0.5-MOF-808.

Deconvolution of experimental d-PDF data:

Multipeak Fit report for Fe-0.5-MOF-808

Total fitted points: 344

Baseline Type: Constant

Table S8.1. Fit report summarize for differential PDF of Fe-1.2-MOF-808.

Peak	1	2	3	4	5	6
Type	Gaussian	Gaussian	Gaussian	Gaussian	Gaussian	Gaussian
Center	1.8	2.01	2.36	2.98	3.33	3.69
Height	0.086642	0.198713	0.169732	0.207713	0.374096	0.128259
Area	0.0212123	0.0655723	0.0289079	0.0442207	0.103535	0.0354971
FWHM	0.23	0.31	0.16	0.22	0.26	0.26
Assignment	Fe-O	Fe-O	Fe-Cl	Fe···Fe	Fe···Fe	Fe···Zr

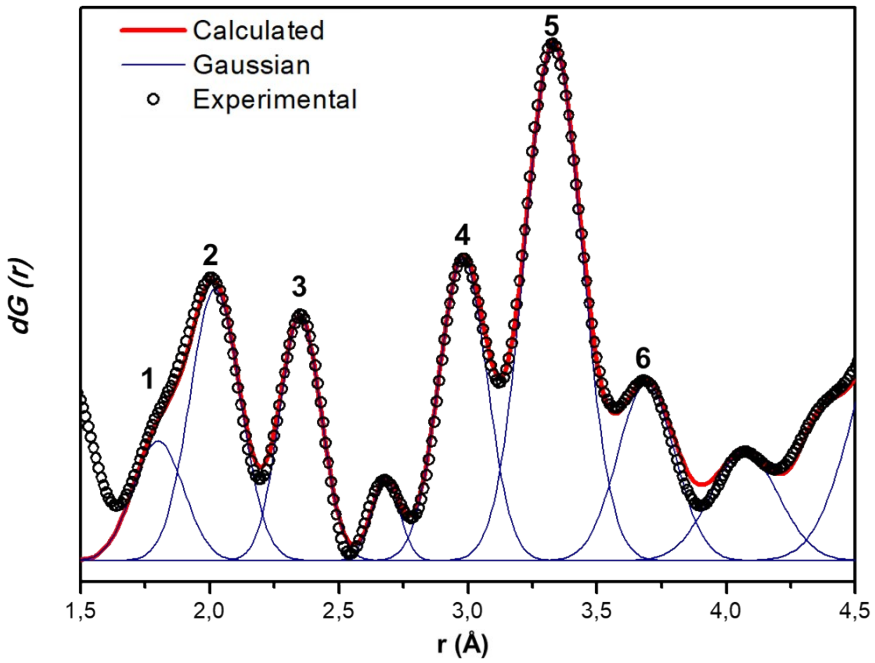

Fig. S8.3. Representative curve fitting for the d-PDF of Fe-0.5-MOF-808. Experimental data (black circles), fit trace (red). Peaks were fit as Gaussian functions (blue).

Multipeak Fit report for dPDF Fe-1.2-MOF-808

Total fitted points: 345

Baseline Type: Constant

Table S8.2. Fit report summarize for differential PDF of Fe-1.2-MOF-808.

Peak	1	2	3	4	5
Type	Gaussian	Gaussian	Gaussian	Gaussian	Gaussian
Center	1.97	2.37	3.00	3.33	3.73
Height	0.13994	0.0896762	0.159035	0.286742	0.102805
Area	0.0327715	0.0152732	0.0423219	0.0702023	0.0207922
FWHM	0.22	0.16	0.25	0.23	0.19
Assignment	Fe-O	Fe-Cl	Fe···Fe	Fe···Fe	Fe···Zr

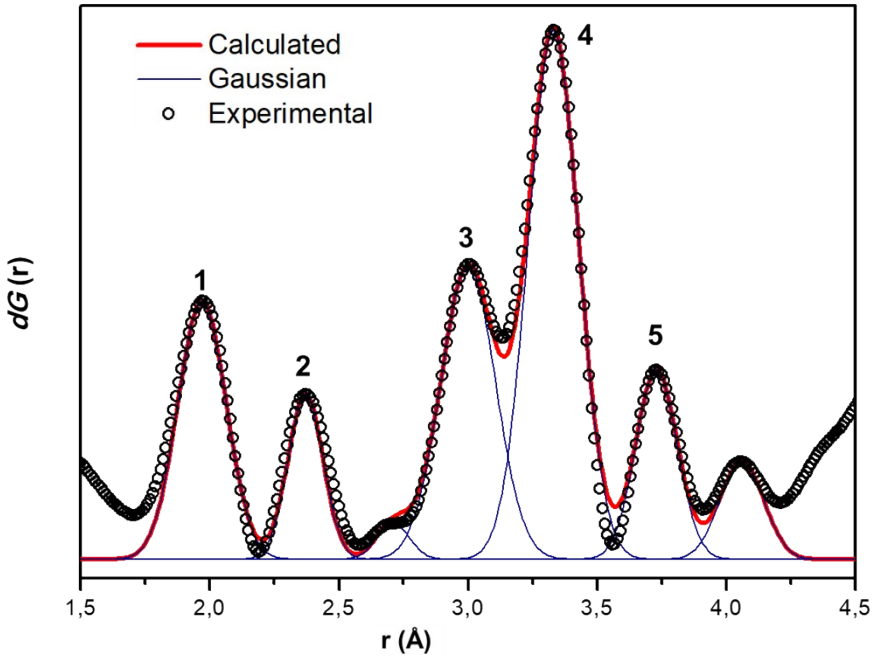

Fig. S8.4. Representative curve fitting for the d-PDF of Fe-1.2-MOF-808. Experimental data (black circles), fit trace (red). Peaks were fit as Gaussian functions (blue).

Peak located at 2.7 Å is a remain of the Fourier Transform.

Deconvolution of simulated iron-oxo clusters data:

Multipeak Fit report for an iron cluster composed by two metallic centers with tetrahedral coordination environmental.

Total fitted points: 989

Baseline Type: Constant

Table S8.3. Fit report summarize for model 1.

Peak	1	2	3	4	5
Type	Gaussian	Gaussian	Gaussian	Gaussian	Gaussian
Center	2.02	2.34	3.04	3.37	3.94
Height	2.48084	1.82894	1.4545	0.526697	0.457954
Area	0.58097	0.564585	0.402549	0.1602589	0.1316
FWHM	0.22	0.29	0.26	0.29	0.27
Assignment	Fe-O	Fe-Cl	Fe···Fe	-	-

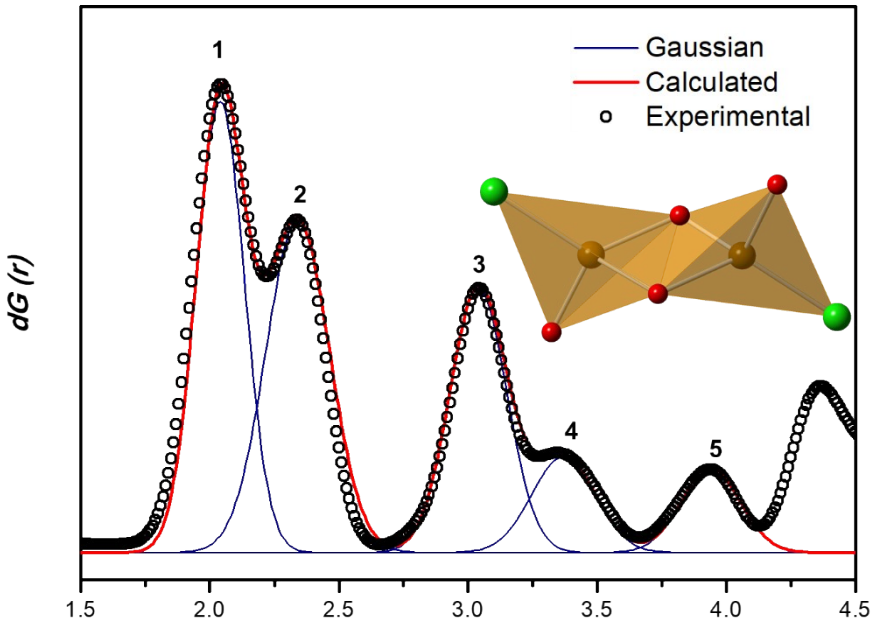

Fig. S8.5. Representative curve fitting for the calculated PDF of od the iron-oxo cluster depicted in the figure inset (red-oxygen, green-chlorine and orange-iron). Calculated data (black circles), fit trace (red). Peaks were fit as Gaussian functions (blue).

Multipeak Fit report for an iron cluster composed by two metallic centers with octahedral coordination environmental.

Total fitted points: 991

Baseline Type: Constant

Table S8.4. Fit report summarize for model 2.

Peak	1	2	3	4	5
Type	Gaussian	Gaussian	Gaussian	Gaussian	Gaussian
Center	2.09	2.34	3.01	3.75	4.20
Height	4.21831	1.57732	3.32179	1.18367	0.446187
Area	1.05478	0.37878	1.10596	0.39272	0.153259
FWHM	0.23	0.22	0.31	0.31	0.32
Assignment	Fe-O	Fe-Cl	Fe···Fe	-	-

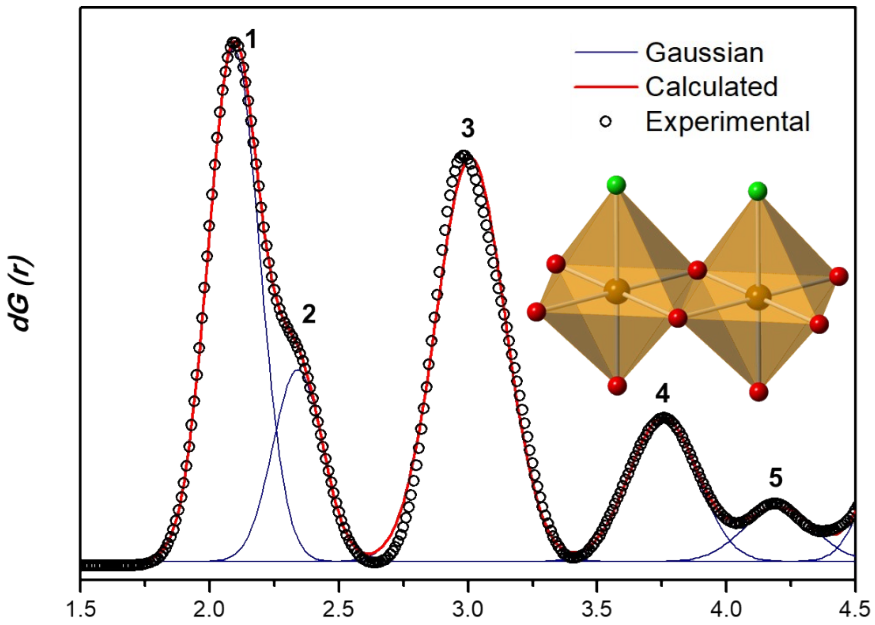

Fig. S8.6. Representative curve fitting for the calculated PDF of od the iron-oxo cluster depicted in the figure inset (red-oxygen, green-chlorine and orange-iron). Calculated data (black circles), fit trace (red). Peaks were fit as Gaussian functions (blue).

Multipeak Fit report for an iron cluster composed by three metallic centers with tetrahedral coordination environmental.

Total fitted points: 351

Baseline Type: Constant

Table S8.5. Fit report summarize for model 3.

Peak	1	2	3	4	5	6
Type	Gaussian	Gaussian	Gaussian	Gaussian	Gaussian	Gaussian
Center	1.99	2.22	3.02	3.66	3.97	4.41
Height	3.37455	1.70968	2.49822	0.352431	0.94250	0.34268
Area	0.79026	0.054597	0.71800	0.071279	0.371206	0.11308
FWHM	0.22	0.30	0.27	0.19	0.37	0.31
Assignment	Fe-O	Fe-Cl	Fe···Fe	-	-	-

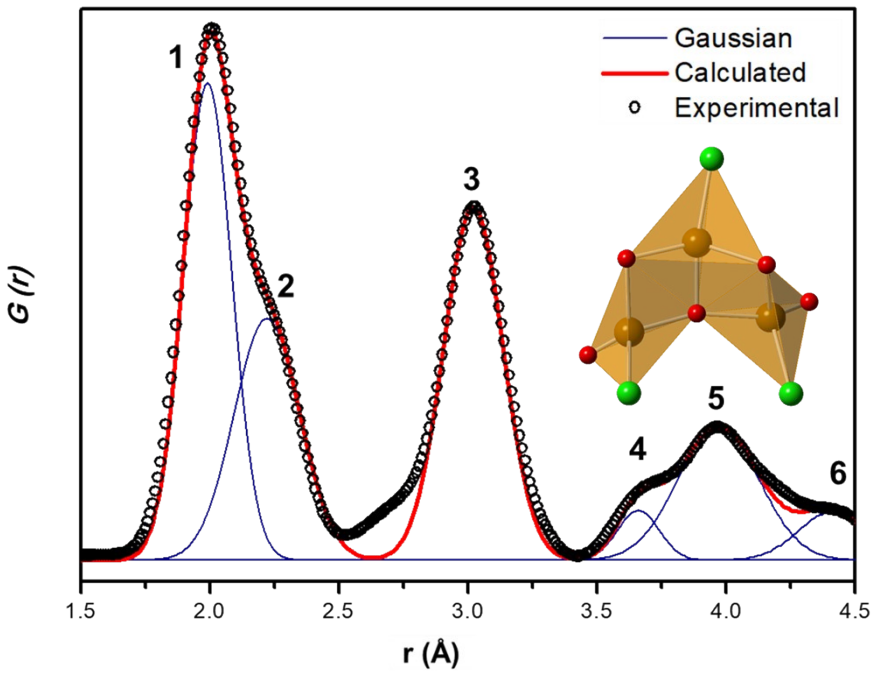

Fig. S8.7. Representative curve fitting for the calculated PDF of od the iron-oxo cluster depicted in the figure inset (red-oxygen, green-chlorine and orange-iron). Calculated data (black circles), fit trace (red). Peaks were fit as Gaussian functions (blue).

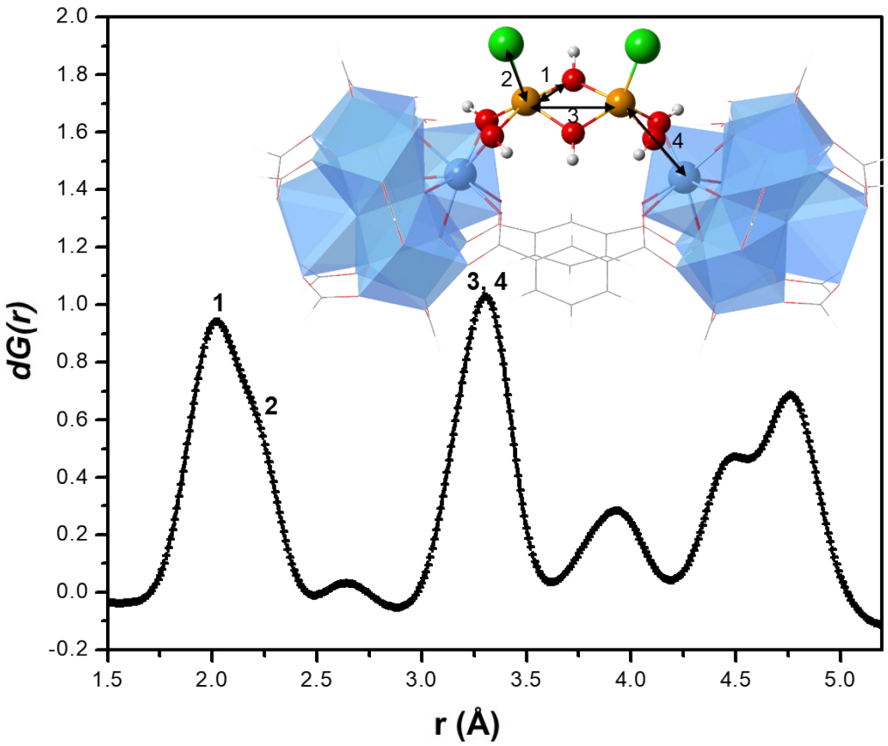

Fig. S8.8. Representative calculated curve for the model A (iron cluster as a bridge between two Zr-nodes). Only the first coordination sphere around the Fe-oxo dimer is calculated.

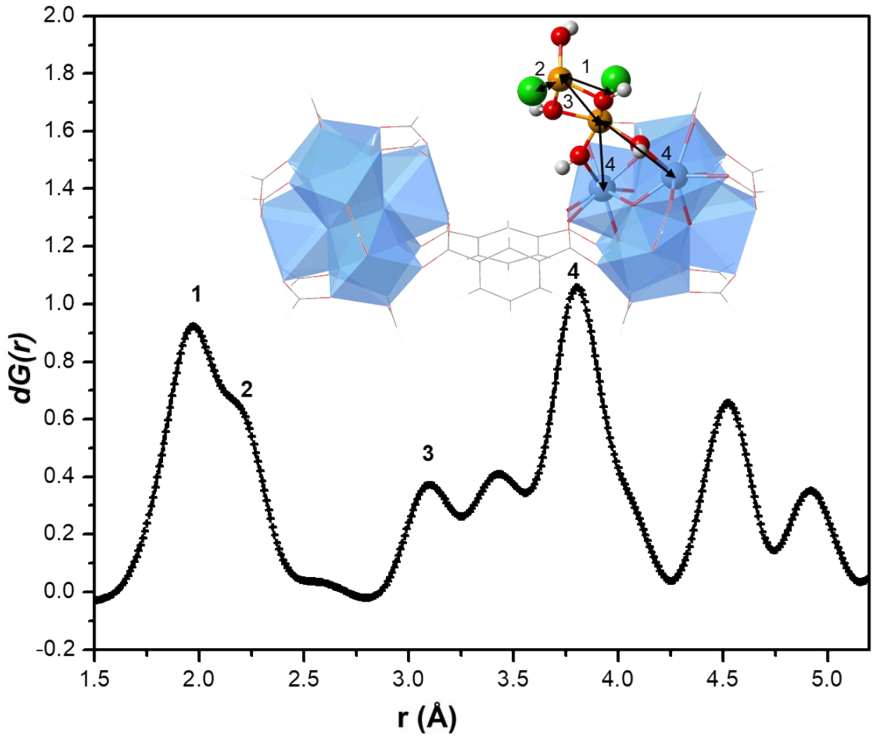

Fig. S8.9. Representative calculated curve for the model B (iron cluster is linked in a terminal position to a Zr-node). Only the first coordination sphere around the Fe-oxo dimer is calculated.

The Fe-oxo dimers bridging two neighnouring Zr-nodes is the main specie according to the simulated PDF of the model in comparison with the dPDF of Fe-0.5-MOF-808 (Figure S8.10). Due to the possible presence of both models, the mixture of both was also calculated.

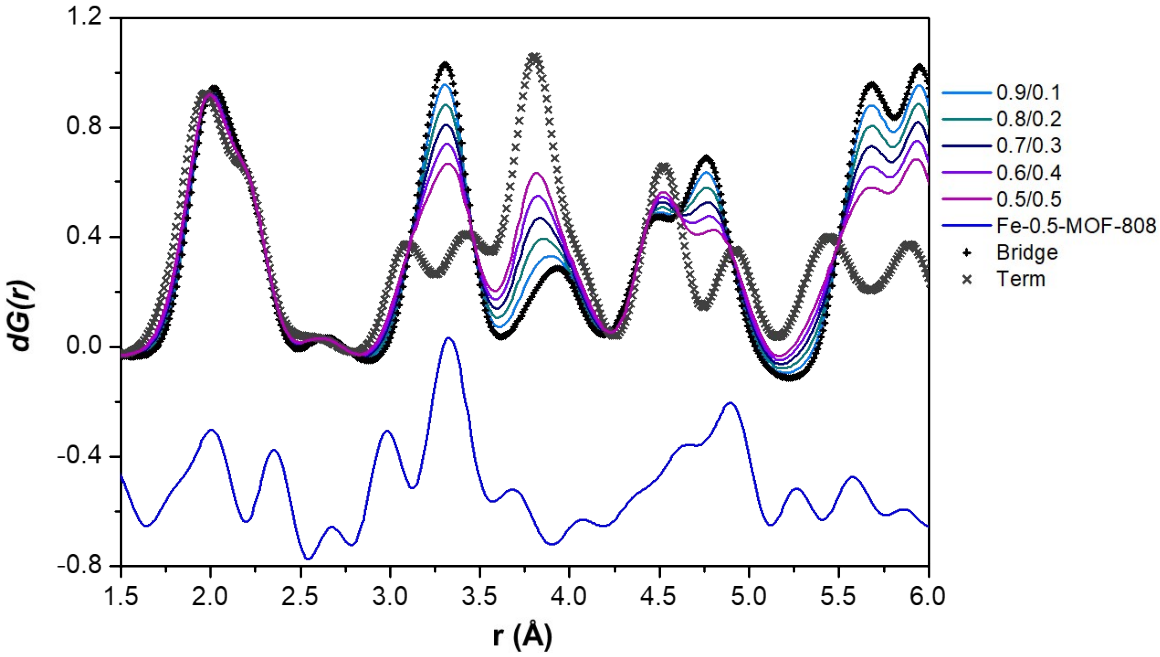

Fig. S8.10. Representative calculated curve for the mixture of both models (A = Bridge, B = Term). The mixtures were depicted as lines with: 90% A, 10% B (cyan); 80% A, 20% B (turquoise); 70% A, 30% B (dark blue); 60% A, 40% B (violet); 50% A, 50%B (pink). dPDF of Fe-0.5-MOF-808 is depicted down (blue).

S9 X-Ray Absorption Spectroscopy

Transmission and fluorescence geometry XAS measurements were performed at CLAESS (BL22) at the ALBA synchrotron. Fe K-edge XAS spectra were acquired from 7100 to 8100 eV, resulting in a k-range up to 10 $Å^{-1}$. The data analysis and background removal were performed within ATHENA and ARTEMIS.[9] Fe_3O_4, $Fe(acac)_3$ and $FeCp_2$ were employed as references.

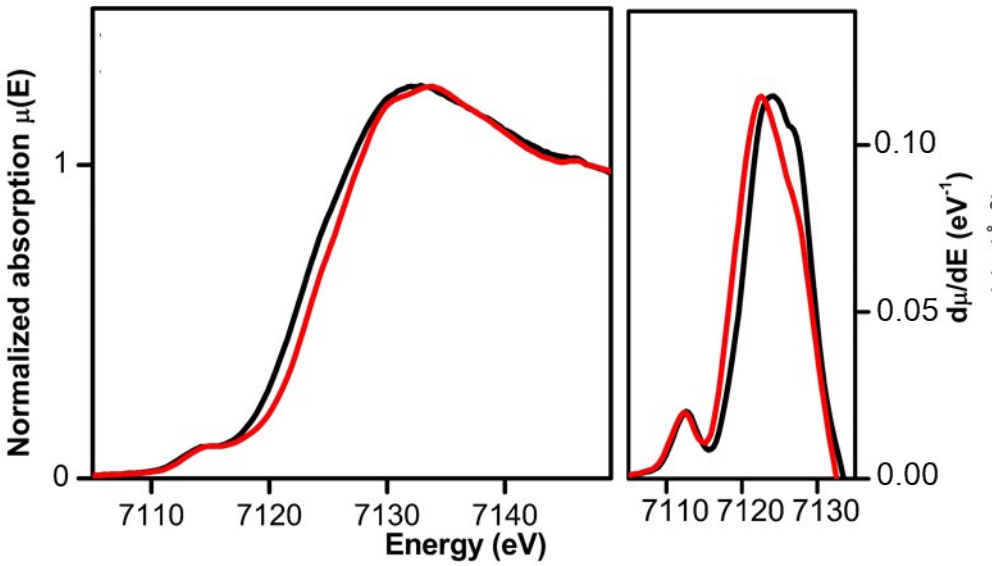

Fig. S9.1. XANES of Fe loaded materials and first derivate analysis (right). Fe-0.5-MOF-808 (black), Fe-1.2-MOF-808 (red).

S10 Computional details

S10.1 Computational methodology

Density Functional Theory (DFT) calculations were performed in order to elucidate the possible conformations of low-loading Fe-MOF-808. We modelled the structural and energetic properties of several binuclear iron-oxo & iron-hydroxo clusters deposited on the nodes of the MOF-808. As a starting model for the pristine MOF-808, we choose a molecular cluster that is composed by two Zr_6O_8 octahedra bridged by 2 ligands. The coordinates of the starting model are carved from the experimentally determined crystal structure. The benzene-tricarboxylate ligands, which are bridging the two Zr_6O_8 octahedra, are cropped to benzene-dicarboxylate. The remaining four ligands are also cropped to formate. Based on the experimental observations, six (6) formate molecules are further added as capping ligands. For charge balancing, four (4) protons have to be added to the μ3-O atoms of each Zr_6O_8 octahedron. The model is shown in Figure S10.1.

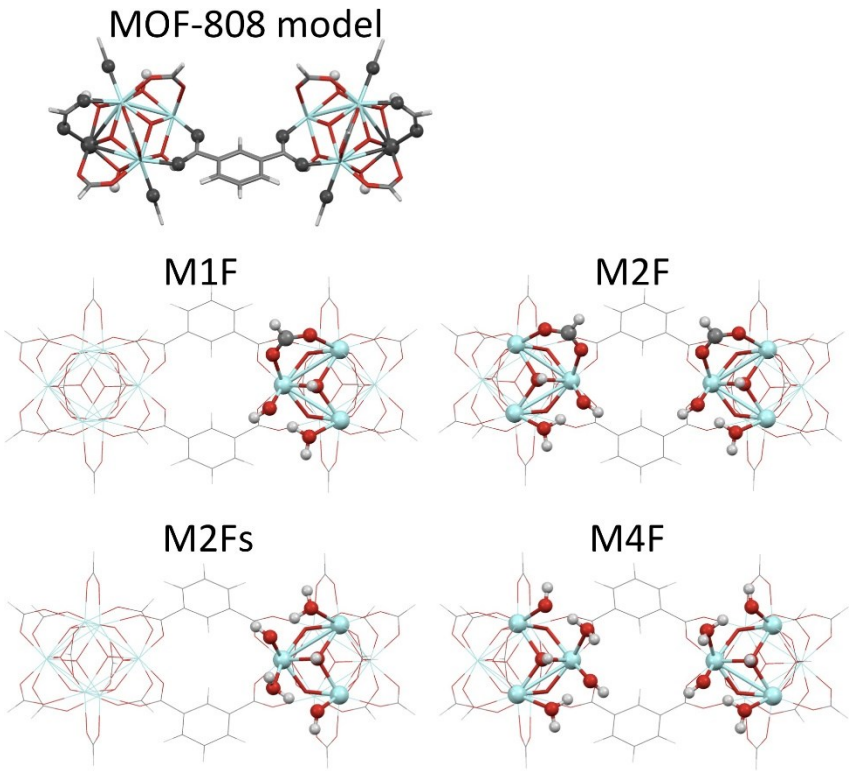

Figure S10.1: Models used in the calculations. (Top) MOF-808 model, where the frozen atoms during the geometry optimizations are shown in dark grey spheres. **M1F**, **M2F** and **M4F** are the MOF models after removing 1, 2 and 4 formate ligands respectively and adding a hydroxo and a water ligand. **M2Fs** is the MOF model after removing 2 formate ligands from the same Zr_6O_8 node.

During all geometry optimizations, some restrictions have to be applied in order to mimic the crystal environment. Two (2) of the zirconium atoms at the edges of the molecular cluster, and the twenty-four (24) oxygen atoms that belong to the ligands are kept frozen. These atoms are shown in dark grey colour in Figure S10.1.

As a next step, one, two or four formate capping ligands are removed, with each one being replaced by a hydroxo and a water molecule, giving rise to the models denoted as

M1F, **M2F**, and **M4F**, respectively. In the case of replacing two formate capping ligands, two possibilities exist: i) replacement of two ligands in the same octahedron (**M2Fs**), or ii) replacement of one ligand in each octahedron (**M2F**). These models are also shown in Figure S10.1.

Subsequently, we investigated the structural and energetic characteristics of the deposition of a $Fe_2Cl_2(\mu_2\text{-}O)_x(OH)_y(H_2O)_z$ cluster on the nodes of the MOF-808 model. We chose to study the $Fe_2Cl_2(\mu_2\text{-}O)_x(OH)_y(H_2O)_z$ cluster based on the experimental observations for the low-loading Fe-MOF-808. To reduce the complexity of the system, due to many possible combinations of Fe(II,III)/Fe(II,III) pairs and the different ways to couple the unpaired electrons of the Fe(II)/Fe(III) atoms, we decided to study only the deposition of the high-spin ferromagnetically coupled Fe(III)-Fe(III) pair with a spin multiplicity of 11. The M06-L[10] method is employed in combination with the 6-31G(d,p) basis set for the C, H, O, Cl and Fe atoms and the SDD for the Zr atoms (along with the appropriate ECPs). Harmonic frequency analysis confirmed structures as minima or saddle points on the potential energy surface. Free energies are calculated based on the harmonic approximation assuming temperatures of 298 K and gas pressures of 1 Atm. All frequencies below 50 cm^{-1} were replaced by 50 cm^{-1} when computing the free energy contribution from the vibrational partition functions. All calculations are performed with the Gaussian 16 software package.[11]

S10.2 Results

Due to the rich proton topology of the MOF-808, several possibilities exist, how a $Fe_2Cl_2(\mu_2\text{-}O)_x(OH)_y(H_2O)_z$ cluster can be deposited on the nodes of the MOF after reaction of the iron-precursor with the available protons from the μ_3-OH, terminal-OH and terminal-Aqua ligands. For example, the iron-precursors may react with: i) the terminal-OH and terminal-Aqua protons giving rise to the conformation **A** (or **Bridging** site), ii) a terminal-Aqua proton giving rise to conformation **B** (or **Terminal** site), and iii) the μ_3-OH and terminal-Aqua protons creating conformation **C** (or **μ_3** site). The lowest energy conformers are presented in Figure SX. For all three conformation, we investigated the deposition of the $Fe_2Cl_2(\mu_2\text{-}O)_x(OH)_y(H_2O)_z$ cluster on all possible models: **M1F**, **M2F**, **M2Fs** , and **M4F**. Furthermore, we have also calculated the free energies of formation of the different conformations by considering a reaction between the MOF-808 model with the $FeCl_3$ (as iron-precursor) and water molecules, which generate the various Fe-MOF-808 conformers and liberate HCl. Detailed information of the computed structures, including formation free energies and Fe-Fe distances, are listed in Table S10.1.

Conformation A: In the conformation **A**, the binuclear iron cluster can be deposited either as $Fe_2Cl_2(\mu_2\text{-}O)_2$ or as $Fe_2Cl_2(\mu_2\text{-}OH)_2$. Depending on the proton topology of the node, several more possibilities exist. They have been calculated and are shown in Figure S10.2.

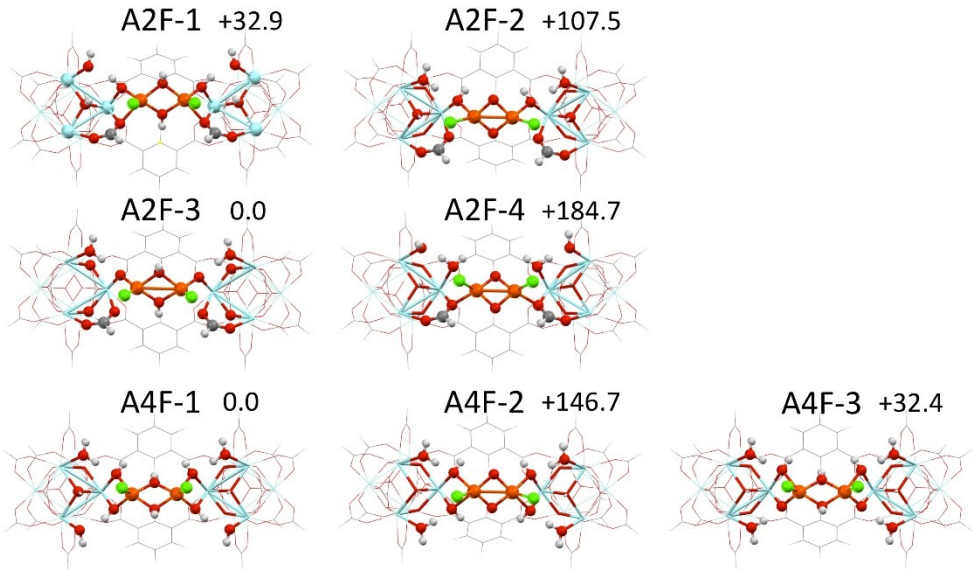

Figure S10.2: Most stable structures of binuclear iron clusters deposited on the Bridging site (Conformation A) of models M2F and M4F. Their relative free energies in kJ/mole are also shown.

In all calculations, the deposition of a $Fe_2Cl_2(\mu_2\text{-}OH)_2$ cluster is more stable than the $Fe_2Cl_2(\mu_2\text{-}O)_2$. Among all possible configurations, the A2F-1 and A2F-3 corresponding to the model M2F and the A4F-1 and A4F-3 from the model M4F are the most stable structures with the most negative formation free energies. They possess Fe…Fe distances between 3.12 and 3.24 Å.

Conformation B: Deposition on the Terminal position is possible after reaction of the iron precursor with the protons from the Aqua ligands. The most negative formation free energies have been calculated for the B1F models at ~-165 kJ/mol, whereas they are slightly higher for the B2Fs models with values between -92 and -147 kJ/mol. The results show that the binuclear iron cluster prefers to get the conformation -$Fe_2Cl_2(\mu\text{-}OH)_2$(t-OH) for the B1F models with Fe…Fe distances at 3.07 Å.

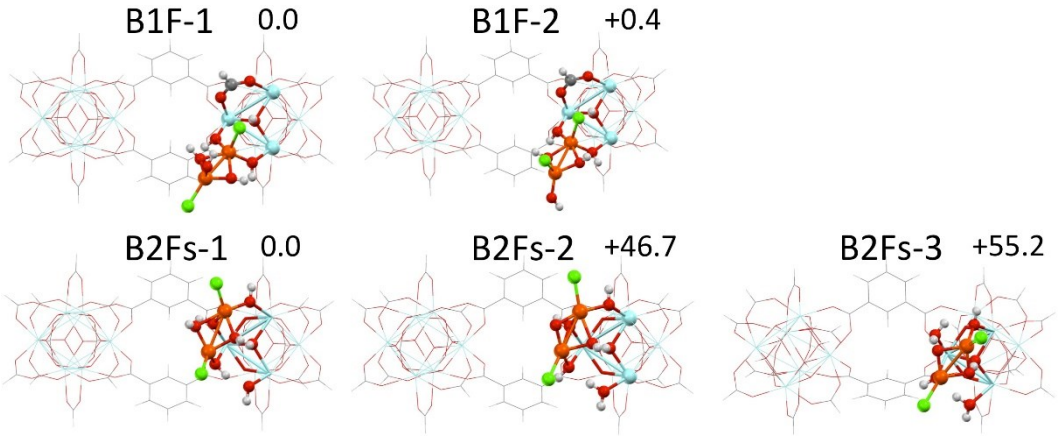

Figure S10.3: Most stable structures of binuclear iron clusters deposited on the Terminal site of the Zr_6O_8 node (Conformation B) of models M1F and M2Fs. Their relative free energies in kJ/mole are also shown.

Conformation C: Deposition on the μ_3-O position is possible after reaction of the μ_3-OH, the t-OH and t-OH_2 protons with the iron precursor. Several structures have been considered and are presented in Figure SX4. In this case, the conformers have the least negative formation free energies among the conformers A and B. The reaction free energies range between -24 and -73 kJ/mol, while the Fe-Fe distances are shorter especially for the C1F models. One of the iron atoms is always bonded to the μ_3-O and is in close proximity to one zirconium atom. One of the chlorine ligands gets a μ_2 configuration between the iron and the zirconium atom from the node. For the C2Fs models, slightly more negative formation free energies are calculated. The models C2Fs-1 and C2Fs-2 possess Fe…Fe distances at ~2.95 Å.

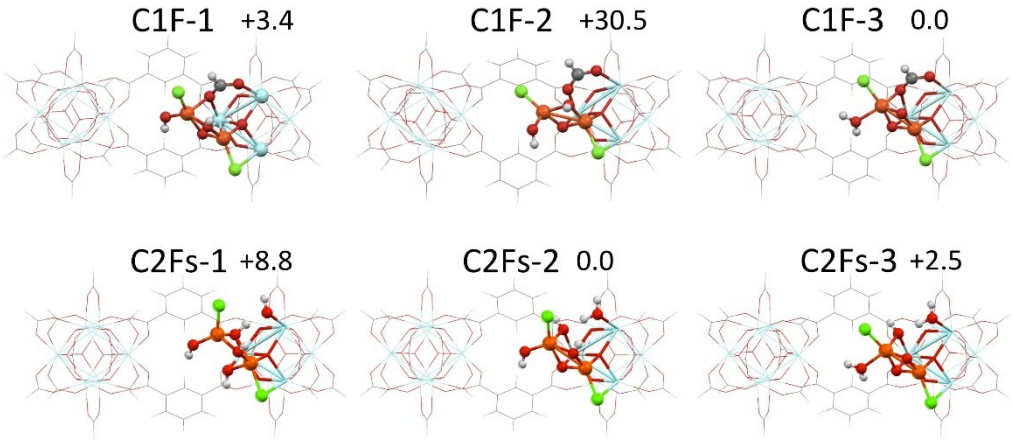

Figure S10.4: Most stable structures of binuclear iron clusters deposited on the μ_3-O site of the Zr_6O_8 node (Conformation C) of models M1F and M2Fs. Their relative free energies in kJ/mole are also shown.

Table S10.1: Summary of results for the different possible conformations of the $Fe_2Cl_2(\mu_2\text{-}O)_x(OH)_y(H_2O)_z$ cluster on the various models of the MOF-808 nodes. The iron-topology is also given along with the proton topology of the nodes. The relative free energies ($\mathbf{\Delta G_{rel}}$ in kJ/mol) are given for the different conformers for the same stoichiometry. The formation free energies ($\mathbf{\Delta G_{form}}$ in kJ/mol) calculated from the reaction: MOF-808 + $2FeCl_3$ + xH_2O → Fe-MOF-808 + 4HCl, are also given along with the Fe-Fe distance (in Å)

	MOF-model	Name	Iron-topology	Proton-topology on the node	ΔG_{rel} (kJ/mol)	ΔG_{form} (kJ/mol)	d(Fe-Fe) (Å)
A - Bridging	M2F	A2F-1	-$Fe_2Cl_2(\mu\text{-}OH)_2$-	(μ3-OH), (t-OH)$_2$	+32.9	-159.0	3.14
		A2F-2	-$Fe_2Cl_2(\mu\text{-}O)_2$-	(μ3-OH), (t-OH), (t-OH_2)	+107.5	-84.4	2.7
		A2F-3	-$Fe_2Cl_2(\mu\text{-}OH)_2$-	(μ3-OH), (t-O), (t-OH_2)	0.0	-191.9	3.12
		A2F-4	-$Fe_2Cl_2(\mu\text{-}O)_2$-	(μ3-OH), (t-OH), (t-OH_2)	+184.7	-7.1	2.67
	M4F	A4F-1	-$Fe_2Cl_2(\mu\text{-}OH)_2$-	(μ3-OH), (t-OH)$_3$, (t-OH_2)	0.0	-221.9	3.20
		A4F-2	-$Fe_2Cl_2(\mu\text{-}O)_2$-	(μ3-OH), (t-OH)$_2$, (t-OH_2)$_2$	+146.7	-75.1	2.74
		A4F-3	-$Fe_2Cl_2(\mu\text{-}OH)_2$-	(μ3-OH), (t-O), (t-OH), (t-OH_2)$_2$	+32.4	-189.5	3.24
B - Terminal	M1F	B1F-1	-$Fe_2Cl_2(\mu\text{-}OH)_2$(t-OH)	(μ3-OH), (t-OH)$_2$	0.0	-165.7	3.07
		B1F-2	-$Fe_2Cl_2(\mu\text{-}OH)_2$(t-OH)	(μ3-OH), (t-OH)$_2$	+0.4	-165.2	3.08
	M2Fs	B2Fs-1	-$Fe_2Cl_2(\mu\text{-}OH)_2$	(μ3-OH), (t-OH)$_4$	0.0	-146.8	2.87
		B2Fs-2	-$Fe_2Cl_2(\mu\text{-}OH)(\mu\text{-}O)$	(μ3-OH), (t-OH)$_3$, (t-OH_2)	+46.7	-100.1	2.71
		B2Fs-3	-$Fe_2Cl_2(\mu\text{-}O)_2$	(μ3-OH), (t-OH)$_2$, (t-OH_2)$_2$	+55.2	-91.6	2.74
C – μ3	M1F	C1F-1	-$Fe_2Cl_2(\mu\text{-}OH)$(t-OH)	(μ3-O), (t-O)	+3.4	-51.4	2.86
		C1F-2	-$Fe_2Cl_2(\mu\text{-}O)_2$	(μ3-O), (t-O)	+30.5	-24.3	2.84
		C1F-3	-$Fe_2Cl_2(\mu\text{-}O)_2$(t-H_2O)	(μ3-O), (t-O)	0.0	-54.7	2.73
	M2Fs	C2Fs-1	-$Fe_2Cl(\mu\text{-}Cl)(\mu\text{-}OH)$(t-OH)	(μ3-O), (t-OH)$_3$	+8.8	-64.0	3.00
		C2Fs-2	-$Fe_2Cl(\mu\text{-}Cl)(\mu\text{-}OH)$(t-OH)	(μ3-O), (t-O), (t-OH), (t-OH_2)	0.0	-72.8	2.95
		C2Fs-3	-$Fe_2Cl(\mu\text{-}Cl)(\mu\text{-}OH)$(t-$H_2O$)	μ3-O), (t-O), (t-OH), (t-OH_2)	+2.5	-70.3	2.74

S11 Capture and catalytic test

BPA remediation experiments were carried out at pH ~ 5.75 in a 10 mL glass sealed vial at 30 °C.

BPA uptake model. MOF-808 (5 mg) was added to a stirred solution of BPA (5 mL, 0.00219 mmol, 100 ppm water:ethanol 95:5). The suspension was stirred at RT for 1h. The suspension was filtered through a 0.22 μm syringe filter. The supernatant was analyzed by HPLC-UV, to calculate the sorption of BPA. The solid was washed twice with 2.5 mL of EtOH, and the filtered through a 0.22 μm syringe filter. The supernatant was analyzed using an Agilent HP1260 Infinity HPLC equipped with a ZORBAX, 4.6 x 100 mm, 3.5 μm C18 column and a UV absorbance detector. A mobile phase of methanol-water (5→95) at a flow rate of 1 mL/min and an injection volume of 20 μL was used for this experiment and the analysis wavelengths were 254, 250 and 210 nm, and the detection limit of BPA in this study was about 0.01 ppm, according to calibration curve (Figure S11.2).

BPA degradation in water through Fenton reactions. Advanced oxidation processes, such as Fenton reactions, are successfully used for the removal of organic pollutants such as bisphenol-A. The Fenton reaction is a catalytic process for the generation hydroxil radicals and is based on electron transfer between hydrogen peroxide and a metal ion. Similarly to previously hypothesized for MIL-88B[12], we propose the following mechanism in Fe-MOF-808 materials:

$$Fe^{III} + H_2O_2 \rightarrow Fe^{II} + {}^{\bullet}OOH + H^+ \quad (1)$$

$$Fe^{II} + H_2O_2 \rightarrow Fe^{III} + {}^{\bullet}OH + OH^- \quad (2)$$

$$Fe^{III} + {}^{\bullet}OOH \rightarrow Fe^{II} + O_2 + H^+ \quad (3)$$

$$\text{Bisphenol A} + {}^{\bullet}OH / \rightarrow \text{degraded products} \quad (4)$$

Two primary steps are involved in this catalytic process: for direct Fenton-like excitation of H_2O_2, H_2O_2 reacts with Fe^{III} located within the cluster to produce Fe^{II} (*Eq.1*), which can further activate H_2O_2 to generate $^{\bullet}OH$ radicals (*Eq.2*). Fe^{II} is recovered from Fe^{III} by *Eq. 3*. The produced $^{\bullet}OH$ radicals are able to react with the bisphenol A, resulting in degradation products (*Eq.4*).

In this work, Fe-MOF-808 (0.04% Fe mmol) was added to a stirred solution of BPA (5 mL, 0.44 mM, 100 ppm water:ethanol 95:5) and hydrogen peroxide (5.55 mg, 0.033 mmol, 30% in water). The beginning of the reaction (t = 0) is determined to be when the catalyst and H_2O_2 are added. The suspension was filtered through a 0.22 μm syringe filter and quenched with sodium thiosulfate. The solid was washed twice with 2.5 mL of EtOH, and the filtered through a 0.22 μm syringe filter and quenched with sodium thiosulfate. The supernatant was analyzed using an Agilent HP1260 Infinity HPLC equipped with a C18 column and a UV absorbance detector. A mobile phase of methanol-water (5→95) at a flow rate of 1 mL/min and an injection volume of 20 μL was used for this experiment and the analysis wavelengths were 254, 250 and 210 nm, and the detection limit of BPA in this study was about 0.1 ppm, according to calibration line.

The difference between the BPA removal, and the BPA released is the BPA degraded.

Blanks experiments for the study of degradation were performed in presence of H_2O_2 and MOF-808 pristine. The amount of BPA degraded was depreciable.

Recycling experiments. Fe-0.5-MOF-808 was reused up to 4 cycles, maintaining the same catalytic activity (Figure S11.3). Each experiment was performed three times to minimize errors. After recovery, the MOF samples were washed with water and acetone, then dried overnight. X-ray diffraction data were collected on the materials after the last catalytic cycle to evaluate crystallinity, purity and recyclability of the MOF (Figure S11.4). PDF data collected on Fe-0.5-MOF-808 after catalysis demonstrated that the short-range order in the MOF is retained (Figure S11.5). The heterogeneous nature of the catalytic process was evaluated through leaching tests using Inductively Coupled Plasma (ICP) analysis, which showed the absence of iron species in solution after the Fenton reaction (Table S11.1).

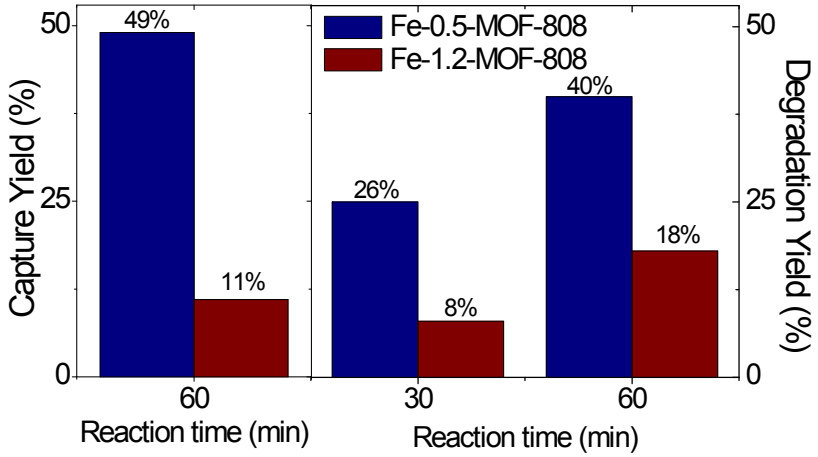

Fig. S11.1. Removal test of 1 mg / 1 mL 100 ppm BPA after 60 min (left), and catalytic degradation, 0.04% molar in Fe over 5 mL of BPA at 100 ppm (right).

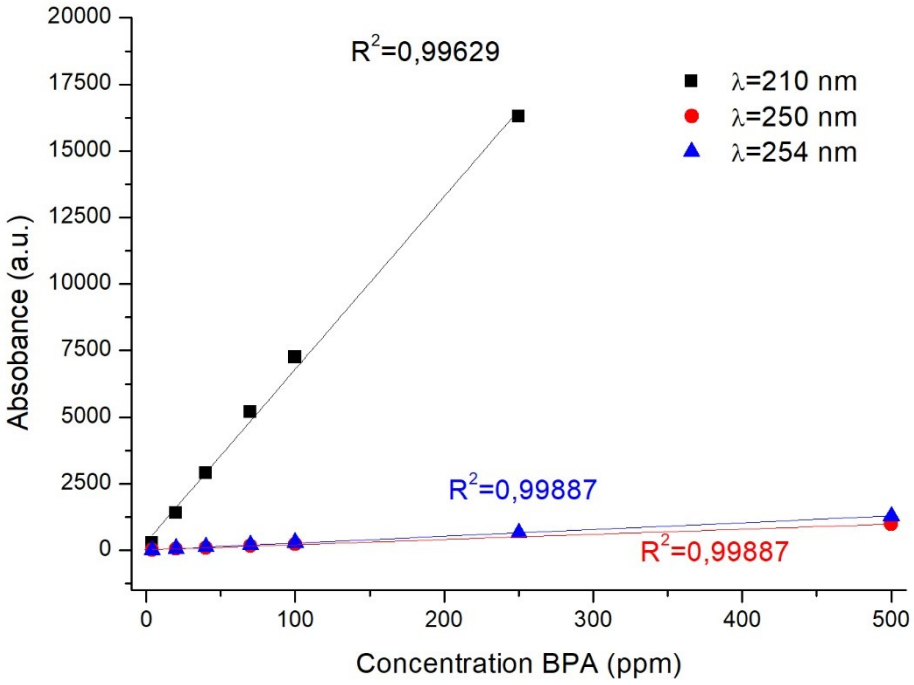

Fig. S11.2. Calibration line for bisphenol-A in methanol as solvent.

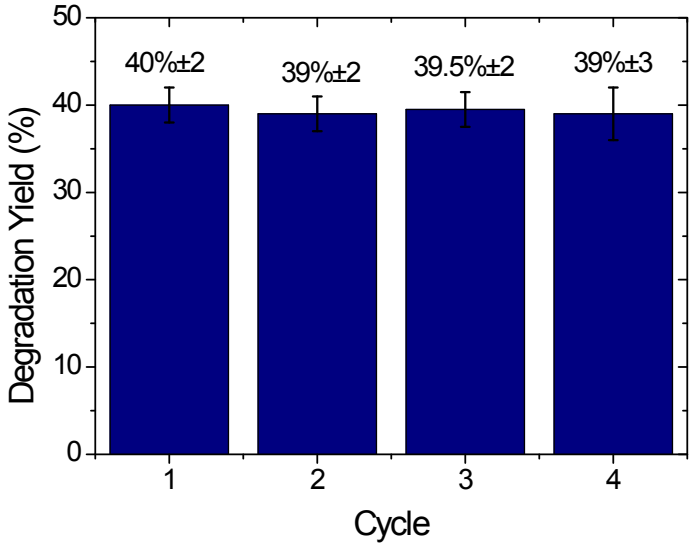

Fig. S11.3. Recyclability test for Fe-0.5-MOF-808 material.

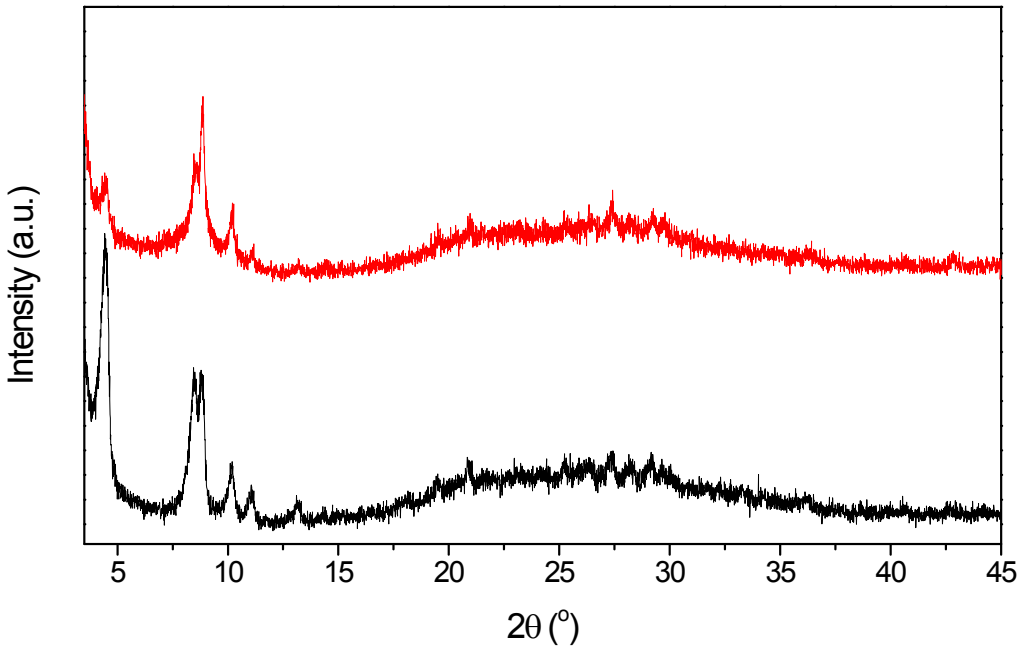

Fig. S11.4. PXRD data for pre-catalytic (black) and post-catalytic (red) Fe-0.5-MOF-808 materials after 4 cycles.

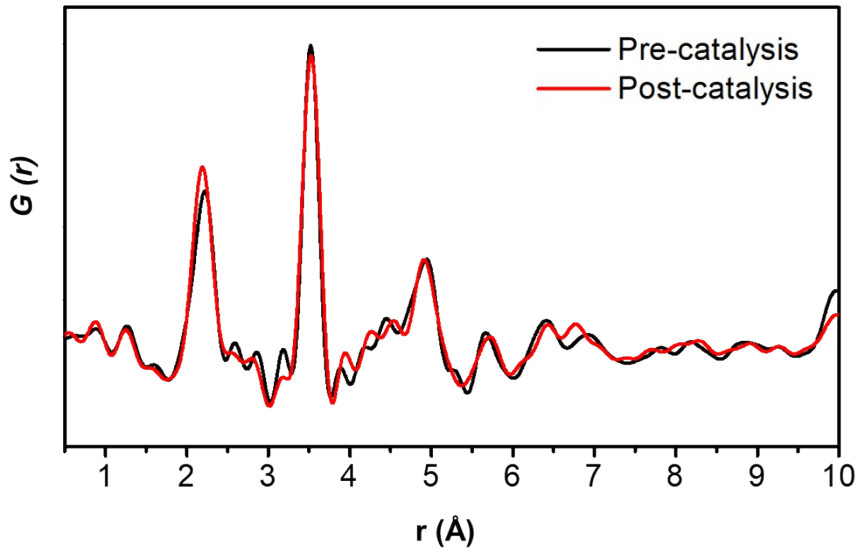

Fig. S11.5. PDF data for pre-catalytic (black) and post-catalytic (red) Fe-0.5-MOF-808 materials.

Table S11.1. ICP analyses of Fe-0.5-MOF-808, pre- and post-catalysis.

Compound	Fe-0.5-MOF-808			
	Zr ppm	Fe ppm	Fe atoms per Zr_6 cluster	%Fe loss
Fe-0.5-MOF-808	80.33	3.51	0.44	-
Fe-0.5-MOF-808 after 4 cycles	78.32	3.48	0.44	0

Comparative analyses:

The degradation of BPA using MOF materials as catalysts typically undergoes through photo-induced Fenton mechanisms, due to the presence of photoactive linkers within the framework. This strategy has been succesfully apply to PCN-222[13] and UiO-66 derivative containing porphirin-based-linkers.[14]

In this work, the object of study is the classic Fenton degradation of BPA using H_2O_2 as generator of hydroxil radicals. In this context, phenol degradation has been also reported using the Fe-MOF MIL-88B as catalysts.[12] Most extended materials employed in this reaction are iron-oxides and iron-oxide composites, as listed in Table S11.2. This table only includes examples of classic Fenton reactions, following a mechanism based in the production of hydroxyl radicals. Fenton mechanisms involving other radicals such as persulfate or peroxymonosulfate are not included in this comparison.

Table S11.2 summarizes the amount of BPA degraded (in mg) per gram of iron within each catalyst, which indicates the activity of the metal centre in the Fenton reaction. As shown in the table, the MOF materials described in this work have excellent activity per iron center, specially Fe-0.5-MOF-808.

Table S11.1. Comparison of different Fe-containing manterials employed as BPA catalysts reported in the literature. Reaction time is in all cases of 1 hour.

Sample	Type of material	Initial pH	BPA:H_2O_2 ratio	Initial BPA concentration (ppm)	% BPA degraded	Fe content (mg)	BPA degraded per g Fe (mg/g)	Fe leaching (mg/L)	Reference
CuFe-MC-1-800	Composite	3	7.6:1	100	93	0.69	144.93	-	[15]
$CuFe_2O_4$	Oxide	5	11.4:1	100	97	23.35	207.71	0.054	[16]
Fe_3O_4	Oxide	5	11.4:1	100	40	36.18	55.28	-	[16]
MS-Fe	Composite	3-9	1:10	0.2	100	13.4	1.49	0	[17]
CFA@Fe_3O_4	Composite	5	1:1	50	90.1	280	160.89	2.2	[18]
Fe_3O_4-Sep	Composite	6	8.5:1	50	98	59.24	84.40	17.4	[19]
Fe-0.5-MOF-808	MOF	5.75	1:1.5	100	40	0.12	331.12	0	This work
Fe-1.2-MOF-808	MOF	5.75	1:1.5	100	18	0.11	169.01	0	This work

S12 Stability tests

The stability of Fe-MOF-808 materials in aqueous media at different pH values was evaluated following a general methodology.[20] For each test, 10 mg of Fe-MOF-808 were suspended in 10 mL of distilled water with different pH values: 3, 7 and 10. pH calibration was performed with a Metrohm 905 Titrando using Scharlab standard solutions of HCl 0.1 N or NaOH 0.1 N, depending on the target pH. After 24 hours, the solids were isolated by centrifugation at 10,000 rpm and washed with water and acetone and then dried under dynamic vacuum. PXRD (Figures S12.1 and S12.2) and ICP analyses (table S12.1) were performed before and after the tests in order to assess both the framework stability and the lack of iron leaching, respectively.

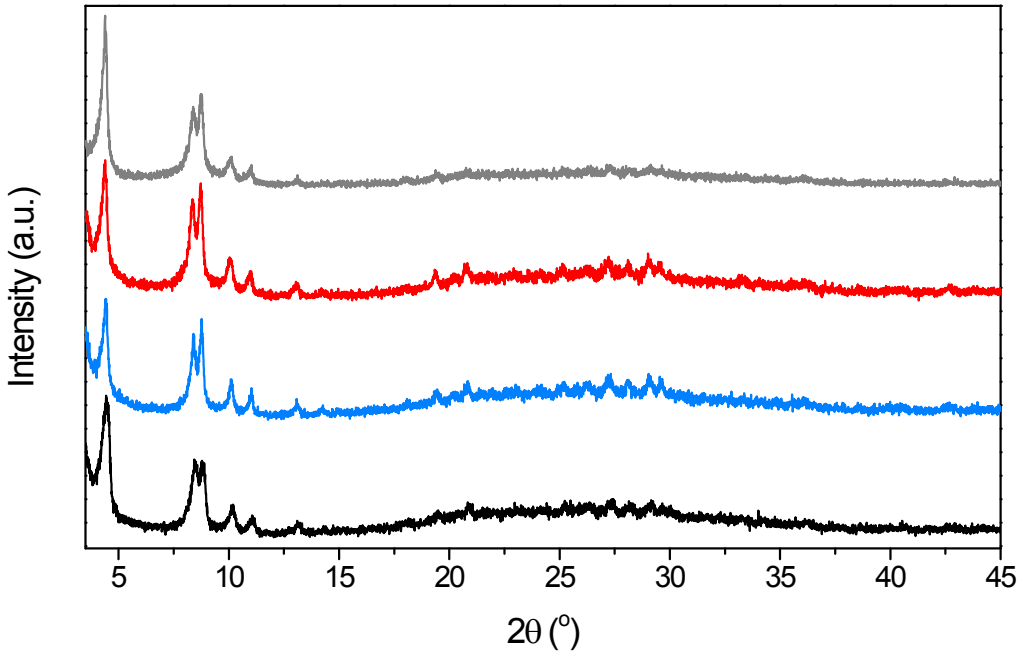

Fig. S12.1. PXRD data before (black) and after stability tests at different pH values: 3 (blue), 7 (red) and 10 (grey) for Fe-0.5-MOF-808 material.

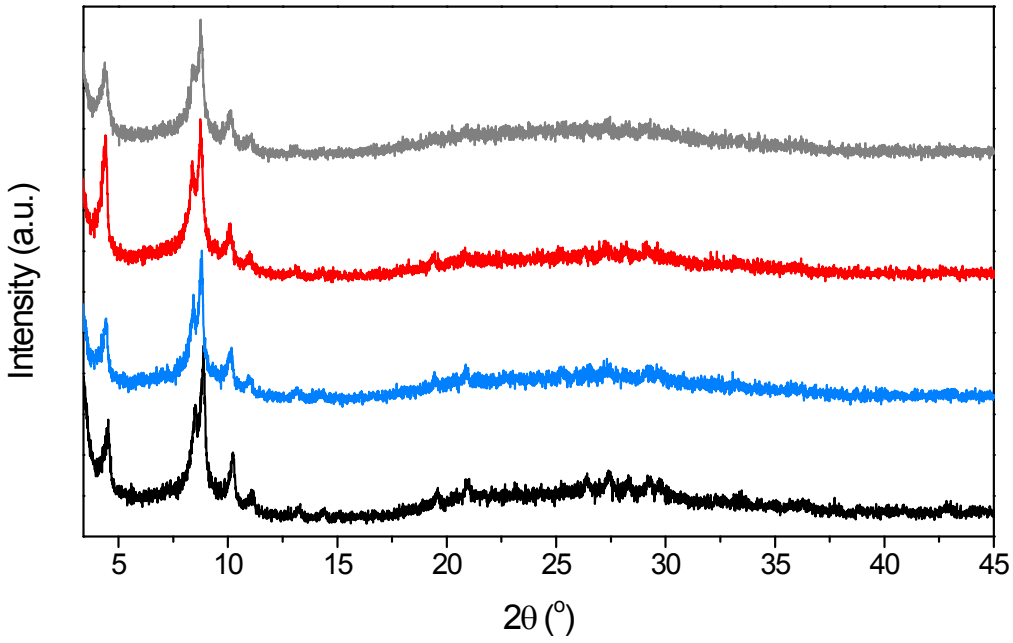

Fig. S12.2. PXRD data before (black) and after stability test at different pH values: 3 (blue), 7 (red) and 10 (grey) for Fe-1.2-MOF-808 material.

Table S12.1. ICP analyses of Fe-0.5-MOF-808 and Fe-1.2-MOF-808 samples before and after stability tests.

pH	Fe-0.5-MOF-808				Fe-1.2-MOF-808			
	Zr ppm	Fe ppm	Fe atoms per Zr_6 cluster	%Fe loss	Zr ppm	Fe ppm	Fe atoms per Zr_6 cluster	%Fe loss
None	80.33	3.51	0.44	-	65.99	7.56	1.18	-
3.00	35.73	1.60	0.44	0	23.49	2.80	1.18	0
7.00	34.55	1.34	0.38	10	26.65	2.90	1.07	5
10.00	34.15	1.36	0.39	9	22.59	2.39	1.04	7

References

1 H. Furukawa, F. Gándara, Y. B. Zhang, J. Jiang, W. L. Queen, M. R. Hudson and O. M. Yaghi, *J. Am. Chem. Soc.*, 2014, **136**, 4369–4381.

2 A. E. Platero-Prats, A. B. League, V. Bernales, J. Ye, L. C. Gallington, A. Vjunov, N. M. Schweitzer, Z. Li, J. Zheng, B. L. Mehdi, A. J. Stevens, A. Dohnalkova, M. Balasubramanian, O. K. Farha, J. T. Hupp, N. D. Browning, J. L. Fulton, D. M. Camaioni, J. A. Lercher, D. G. Truhlar, L. Gagliardi, C. J. Cramer and K. W. Chapman, *J. Am. Chem. Soc.*, 2017, **139**, 10410–10418.

3 J. He, Y. Zhang, X. Zhang and Y. Huang, *Sci. Rep.*, 2018, **8**, 5159 (1–8).

4 M. Basham, J. Filik, M. T. Wharmby, P. C. Y. Chang, B. El Kassaby, M. Gerring, J. Aishima, K. Levik, B. C. A. Pulford, I. Sikharulidze, D. Sneddon, M. Webber, S. S. Dhesi, F. Maccherozzi, O. Svensson, S. Brockhauser, G. Náray and A. W. Ashton, *J. Synchrotron Radiat.*, 2015, **22**, 853–858.

5 P. Juhás, T. Davis, C. L. Farrow and S. J. L. Billinge, *J. Appl. Crystallogr.*, 2013, **46**, 560–566.

6 M. Wojdyr, *J. Appl. Crystallogr.*, 2010, **43**, 1126–1128.

7 Accelrys Inc., BIOVIA Materials Studio.

8 C. L. Farrow, P. Juhas, J. W. Liu, D. Bryndin, E. S. Boin, J. Bloch, T. Proffen and S. J. L. Billinge, *J. Phys. Condens. Matter*, 2007, **19**, 335219 (1–7).

9 B. Ravel and M. Newville, in *Journal of Synchrotron Radiation*, 2005, pp. 12 (4), 537–541.

10 Y. Zhao and D. G. Truhlar, *J. Chem. Phys.*, 2006, **125**, 194101 (1–18) .

11 M. J. Frisch, G. W. Trucks, H. B. Schlegel, G. E. Scuseria, M. A. Robb, J. R. Cheeseman, G. Scalmani, V. Barone, G. A. Petersson, H. Nakatsuji, X. Li, M. Caricato, A. V. Marenich, J. Bloino, B. G. Janesko, R. Gomperts, B. Mennucci, H. P. Hratchian, J. V. Ortiz, A. F. Izmaylov, J. L. Sonnenberg, D. Williams-Young, F. Ding, F. Lipparini, F. Egidi, J. Goings, B. Peng, A. Petrone, T. Henderson, D. Ranasinghe, V. G. Zakrzewski, J. Gao, N. Rega, G. Zheng, W. Liang, M. Hada, M. Ehara, K. Toyota, R. Fukuda, J. Hasegawa, M. Ishida, T. Nakajima, Y. Honda, O. Kitao, H. Nakai, T. Vreven, K. Throssell, J. A. Montgomery, J. E. P. Jr., F. Ogliaro, M. J. Bearpark, J. J. Heyd, E. N. Brothers, K. N. Kudin, V. N. Staroverov, T. A. Keith, R. Kobayashi, J. Normand, K. Raghavachari, A. P. Rendell, J. C. Burant, S. S. Iyengar, J. Tomasi, M. Cossi, J. M. Millam, M. Klene, C. Adamo, R. Cammi, J. W. Ochterski, R. L. Martin, K. Morokuma, O. Farkas, J. B. Foresman and D. J. Fox, 2016, Gaussian 16, Revision B.01.

12 X. Liao, F. Wang, F. Wang, Y. Cai, Y. Yao, B. T. Teng, Q. Hao and L. Shuxiang, *Appl. Catal. B Environ.*, 2019, **259**, 118064 (1-11).

13 A. N. Meng, L. X. Chaihu, H. H. Chen and Z. Y. Gu, *Sci. Rep.*, 2017, **7**, 6297 (1-9).

14 L. Wang, P. Jin, S. Duan, J. Huang, H. She, Q. Wang and T. An, *Environ. Sci. Nano*, 2019, **6**, 2652-2661 .

15 Y. Wang, H. Zhao and G. Zhao, *Appl. Catal. B Environ.*, 2015, **164**, 396-406 .

16 X. Zhang, Y. Ding, H. Tang, X. Han, L. Zhu and N. Wang, *Chem. Eng. J.*, 2014, **236** , 251-262.

17 J. Du, J. Bao, X. Fu, C. Lu and S. H. Kim, *Appl. Catal. B Environ.*, 2016, **184**, 132-141.

18 X. Xu, S. Zong, W. Chen and D. Liu, *Chem. Eng. J.*, 2019, **369**, 470-479.

19 X. Xu, W. Chen, S. Zong, X. Ren and D. Liu, *Chem. Eng. J.*, 2019, **373**, 140-149.

20 A. J. Howarth, A. W. Peters, N. A. Vermeulen, T. C. Wang, J. T. Hupp and O. K. Farha, *Chem. Mater.*, 2017, **29**, 26-39.